

UC Berkeley

UC Berkeley Electronic Theses and Dissertations

Title

Structure of the activated ROQ1 resistosome directly recognizing the pathogen effector XopQ

Permalink

<https://escholarship.org/uc/item/0230f5hv>

Author

Martin, Raoul Olivier

Publication Date

2021

Peer reviewed|Thesis/dissertation

Structure of the activated ROQ1 resistosome directly recognizing the pathogen effector
XopQ

By

Raoul O. Martin

A dissertation submitted in partial satisfaction of the
requirements for the degree of
Doctor of Philosophy
in
Biophysics
in the
Graduate Division
of the
University of California, Berkeley

Committee in charge:

Professor Eva Nogales, Chair
Professor John Kuriyan
Professor Andreas Martin
Professor Russell Vance

Spring 2021

Structure of the activated ROQ1 resistosome directly recognizing the pathogen effector

XopQ

©2021

By

Raoul Martin

Abstract

Structure of the activated ROQ1 resistosome directly recognizing the pathogen effector XopQ

By

Raoul O. Martin

Doctor of Philosophy in Biophysics

University of California, Berkeley

Professor Eva Nogales, Chair

Plants and animals respond to pathogen invasion via intracellular nucleotide-binding leucine-rich repeat receptors (NLRs) that directly interact with pathogen proteins or indirectly detect pathogen-derived alterations of the host proteome. Upon recognition of pathogen invasion, NLRs trigger an immune response that resolves in a variety of ways depending on the type of NLR being activated. The overall architecture of NLRs is highly conserved, consisting of an C-terminal LRR platform that determines substrate specificity and a central nucleotide-binding oligomerization domain. The N-terminal domain varies among NLRs and determines the mechanism utilized by the host to activate the immune response. In plants, NLRs have been classified according to their N-terminal domains: TNLs (TIR-NLRs), CNLs (CC-NLRs) and RNLs (CC_R-NLRs). Pathogen detection and oligomerization of the NLR activates these N-terminal domains by bringing them in close-contact. In all 3 cases, association of the N-terminal domain leads to localized cell death and expression of disease resistance. While the TIR domains of TNLs have been shown to possess oligomerization-dependent NADase activity, it is not understood how their association leads to activation.

The structure of the ROQ1-XopQ complex, a TNL immune receptor bound to its pathogen substrate, was used as a model to study the mechanism of direct effector recognition, oligomerization, and TIR domain activation. ROQ1 has been shown to physically interact with the *Xanthomonas* effector XopQ, causing it to oligomerize and trigger a TIR-dependent hypersensitive cell death response. We co-expressed, extracted and purified the assembled ROQ1-XopQ complex from ROQ1's native host, *Nicotiana benthamiana*, and solved its structure by cryo-EM to 3.8 Å resolution. The interactions described in our structure were further confirmed by in vivo mutational analysis.

Our structure reveals that ROQ1 forms a tetrameric resistosome upon recognizing XopQ. The LRR and a post-LRR domain, termed C-JID (C-terminal Jelly-roll/Ig-like Domain), form a horseshoe shaped scaffold that curls around the pathogen effector, thereby

recognizing multiple regions of the substrate. Roq1 binds to XopQ via surface exposed residues that make up the LRR scaffold as well as an elongated loop between two leucine-rich repeats that forms a small amphipathic α -helix at the site of interaction. The mode of substrate recognition utilized by the C-JID is reminiscent of the way immunoglobulins bind to their antigen. Similarly to the complementary-determining regions of antibodies, interconnecting loops emerging from the C-JID β -sandwich structure make substrate-specific contacts with XopQ. In particular, an extended loop of the C-JID dives into the active site cleft of XopQ and interacts with conserved residues required for nucleoside binding, suggesting that ROQ1 not only recognizes its substrate but also inhibits its ligand-binding function. The NB-ARC domain (NBD, HD1, WHD) of ROQ1 responsible for oligomerization is found in an ATP-bound state. Individual protomers intercalate in a similar fashion as found in other NLR structures, promoting association between the N-terminal TIR domains. The TIR domains bind to each other via two distinct interfaces (termed AE and BE) causing them to form a dimer of dimers. BE-interface contacts cause a conformational rearrangement in a loop, termed the BB-loop, at the periphery of the TIR domain active site that exposes the putative catalytic glutamate, suggested to participate in NAD^+ cleavage. These results provide a rationale for the previously determined oligomerization-dependence of TIR domain NADase activity.

A step-by-step mechanism for ROQ1 immune signaling is proposed based on our structure of the activated complex and previous biochemical studies. The LRR and C-JID of ROQ1 recognize the pathogen effector via direct contacts with its surface and active site residues. Detection of the substrate releases autoinhibitory contacts between the NB-ARC domain and the LRR allowing the NB-ARC domain to transition to an ATP-bound oligomerization prone state. Complex assembly brings the TIR domains in close contact leading to opening of the NADase active site in an interface-dependent manner.

Dedication

To my mother, Rebecca Tagett, who always believed in me.

Acknowledgements

My favorite part of graduate school has been the close relationships I have made with extraordinary people. First and foremost, I would like to thank Kirsten Verster, whose love, patience and support was essential to my journey. Starting a small family in the University Village with Kirsten and Pooch was one of the best decisions I've ever made. Thank you Lisa Eshun-Wilson, my lab sibling, for her camaraderie and infectious optimism. Growing together as scientists is my most cherished experience in the Nogales lab. I also want to thank all the friends I've made over these last 6 years – mainly Robert Rietmeijer, Ryan Zarcone, Julian Hassinger, Bob Cail, Chris Habrian, Sam Itskanov, Christian Diercks, Robinson Flaig, Kyle Cordova, Mathieu Prévot, Francisco Hidalgo, Ben LaFrance and Nicole Haloupek. You all contributed to my happiness and to who I am today.

With respect to research itself, I thank my advisor Eva Nogales and members of the Nogales lab (Patricia Grob, Teresa Tucker, Jie Fang, Abhiram Chintangal, Dan Toso, Paul Tobias, Basil Greber and Liz Kellogg) for their support and providing me the tools and expertise necessary to explore the field of cryo-EM. It was a privilege doing so in such an elite environment. Thank you to Brian Staskawicz, Tiancong Qi and Furong Liu for introducing me to plant pathology and patiently answering all of my questions as I learned about an entirely new field in the last two years of my Ph.D. Brian became a second advisor to me and his sports coach-like character was exactly what I needed to push through the finish line. I also would like to thank my dissertation committee, Andreas Martin, John Kuriyan, Russell Vance, in addition to Kate Chase, the Biophysics program administrator, for their advice and for forging my path to becoming a scientist.

Finally, I want to thank Fred Amenta, Phil Koldewey, Scott Horowitz and James Bardwell, the mentors that are responsible for introducing me to research as an undergraduate student.

Table of Contents

Abstract	1
Dedication	i
Acknowledgements	ii
Table of Contents	iii
List of Figures	v
Chapter One: The role of TIR-NLRs in plant immunity and the overall structure of the ROQ1-XopQ complex	1
1.1 Introduction	1
1.1.1 The role of NLRs in plant immunity	1
1.1.2 State of the field	1
1.1.3 The ROQ1-XopQ complex as a model for studying TNLs and direct effector recognition	2
1.2 Results and discussion	2
1.2.1 Insights from the ROQ1-XopQ complex purification	3
1.2.2 Insights from the cryo-EM sample preparation, data collection and processing	4
1.2.3 The overall structure of the ROQ1-XopQ complex	5
1.3 Conclusion	7
1.4 Materials and Methods	8
1.4.1 Plant Materials and Growth Conditions	8
1.4.2 Expression and purification of the ROQ1-XopQ complex	8
1.4.3 Sample Preparation for Cryo-EM	8
1.4.4 Data Collection	9
1.4.5 Data Processing	9
1.4.5 Model Building and Refinement	12
1.4.6 HR phenotype and co-immunoprecipitation	13
1.4.7 Data Deposition	13
Chapter Two: Recognition of the pathogen effector XopQ by ROQ1	16
2.1 Introduction	16
2.2 Results and Discussion	16
2.2.1 Substrate recognition by the LRR	16
2.2.2 Characterization of the Post-LRR domain	17
2.2.3 Substrate recognition by the C-JID	19
2.2.4 Conservation of the ROQ1 C-JID	21
2.3 Conclusion	21
2.4 Materials and Methods	22
2.4.1 Cryo-EM data processing	22
2.4.2 Model building and refinement	22
2.4.3 Residue conservation in the ROQ1 C-JID	23
Chapter Three: Oligomerization of ROQ1	24

3.1 Introduction	24
3.2 Results and Discussion	24
3.2.1 Auto-inhibition and activation of ROQ1	24
3.2.2 ATP-binding	24
3.2.3 Oligomerization interface	25
3.2.4 Mechanism of oligomerization	27
3.3 Conclusions	28
3.4 Materials and Methods	28
Chapter Four: TIR domain association and activation	29
4.1 Introduction	29
4.2 Results and Discussion	29
4.2.1 TIR domains assemble in a dimer of dimers conformation	29
4.2.2 BB-loop conformational rearrangement	32
4.2.3 NADase activity	33
4.3 Conclusions	35
4.4 Materials and Methods	35
2.4.1 Cryo-EM data processing	35
2.4.2 Model building and refinement	37
Chapter Five: Final conclusions and outlook	38
References	39

List of Figures

Figure 1.1 Purification trials leading to our successful protocol.	3
Figure 1.2 Steps in the purification of the ROQ1-XopQ complex visualized by silver stained SDS-PAGE.	4
Figure 1.3 Sample application onto a cryo-EM grid coated with a layer of amorphous carbon.	5
Figure 1.4 Overall structure of the ROQ1-XopQ complex.	7
Figure 1.5 Cryo-EM data processing tree from collected EM movies to the initial reconstruction of the ROQ1-XopQ complex.	11
Figure 1.6 Resolution estimation.	12
Supplementary Table 1.1 Data collection, 3D reconstruction, and refinement statistics.	14
Supplementary Figure 1.1 HR Phenotype and Protein Expression of ROQ1 mutants.	15
Figure 2.1 Structure of the ROQ1 LRR binding to XopQ.	17
Figure 2.2 Comparison between the ROQ1 C-JID (PL domain) and the RPP1 C-JID.	18
Figure 2.3 Structure of the ROQ1 C-JID (PL domain) binding to XopQ.	20
Figure 2.4 Similar mode of recognition utilized by the C-JID and immunoglobulins.	20
Figure 2.5 Residue conservation of the ROQ1 C-JID.	21
Figure 2.6 Focused refinement of the ROQ1-XopQ interaction region.	22
Figure 2.7 Resolution estimation.	22
Figure 3.1 The ATP-binding site of the ROQ1 NB-ARC domain.	25
Figure 3.2 Oligomerization interfaces between NB-ARC domains.	26
Figure 3.3 Structure of the NBD N-terminal linker in activated NLRs with increasing oligomeric states.	27
Figure 4.1 TIR domain interfaces.	31
Figure 4.2 TIR domain conformational rearrangement of the BB-loop.	33
Figure 4.3 A small unidentified density is observed above the TIR domain active site.	34
Figure 4.4 Further cryo-EM data processing needed to resolve the TIR domains.	36
Figure 4.5 Resolution estimation.	37
Figure 5 Hypothetical mechanism of ROQ1 activation.	38

Chapter One

The role of TIR-NLRs in plant immunity and the overall structure of the ROQ1-XopQ complex

Note: These results have been published and are discussed in more detail in our recent paper Martin et al. 2020 (1).

1.1 Introduction

1.1.1 The role of NLRs in plant immunity

Plants have a highly evolved and finely-tuned innate immune system that recognizes invading phytopathogens to protect themselves from infection and disease. Specific pathogen recognition is facilitated by both membrane-anchored pattern recognition receptors that recognize common features shared among pathogens and by intracellular innate immune receptors that detect secreted effectors in the cytoplasm. The latter includes as a major class the nucleotide binding leucine-rich repeat receptors (NLRs) (2). While some NLR immune receptors directly bind pathogen cognate effector proteins, others monitor effector-mediated alterations of host targets to activate effector-triggered immunity (ETI) (3–8). ETI activation is often accompanied by a localized cell death referred to as the hypersensitive response (HR). Animals also employ NLR proteins as intracellular immune receptors to recognize potential pathogens (9) and the NLR domain architecture is highly conserved, with each region playing a specific role in its mechanism of action. Plant NLRs generally consist of three main domains: an N-terminal region that is either a coiled-coil (CC) domain or a Toll/interleukin 1 receptor (TIR) domain, a central nucleotide binding NB-ARC domain that is shared by Apaf-1, plant R proteins and CED-4, and the C-terminal leucine-rich repeat (LRR) domain (2). Plant NLRs are mainly divided into TIR-NLRs (TNLs) and CC-NLRs (CNLs) based on their N-terminal domains, with experimental evidence consistently suggesting that the TIR and CC domains function in signal transduction and ETI activation in a way that is dependent on their oligomerization (3).

1.1.2 State of the field

Until recently, progress on understanding the molecular basis of how plant NLRs are activated had been limited, in large part due to the difficulty isolating NLR soluble recombinant protein and their low levels in native tissue. In 2019, a cryo-EM study revealed how one class of NLR resistosomes is activated (10, 11). HopZ-Activated Resistance1 protein (ZAR1), a CC-NLR identified in *Arabidopsis thaliana*, forms a complex with the Resistance-Related Kinase1 (RKS1) pseudokinase to facilitate immunity by indirectly recognizing the *Xanthomonas campestris* pv. *campestris* type III effector AvrAC. AvrAC uridylylates the receptor-like cytoplasmic kinase PBL2, which is then recognized by RKS1 in the preformed ZAR1–RKS1 complex, resulting in oligomerization and formation of a pentameric resistosome. Once activated, the ZAR1

resistosome displays a funnel-shaped structure formed by oligomerization of the very N-terminal amphipathic α helix, which has been proposed to insert into the plasma membrane forming a pore that promotes immune response by disrupting membrane permeability acting as an ion channel.

Elucidation of the ZAR1 CC-NLR resistosome was a milestone for the field of plant immunity, but does not provide us with any insight into the mechanism of TIR-NLR activation. The N-terminal TIR and CC domains are completely different, and there is still no structural evidence for TIR-NLRs resistosome formation. Recently, TIR domains of both plant and animal NLRs were reported to possess NAD⁺ cleaving capability that requires TIR domain oligomerization to result in NADase activity and immune response activation (12, 13). Whether the NADase activity of the TIR domain is fully responsible for ETI activation, and why NAD⁺ cleaving only happens in the presence of TIR self-association still requires further investigation. In addition, the mechanistic details of NAD⁺ cleavage and product formation remain unresolved and have been found to vary among TIR domains (13). The steps in this enzymatic reaction involve breaking the glycosidic bond that connects nicotinamide to ADPR and, in some cases, a structural rearrangement in ADPR that leads to the formation of cyclic-ADPR or variant-cyclic-ADPR (13, 14). These products have been shown to modulate Ca²⁺ level in plant cells, which is a widely used chemical signal for responding to various biotic and abiotic stresses. (15–18). Furthermore, it is known that all plant TIR-NLRs require the downstream EDS1 and either PAD4 or SAG 101 and NRG1 proteins to achieve cell death (19–23). The TIR-dependent immune signal could be transmitted via products of NADase activity or direct interaction with complexes of the EDS1 family, as well as helper NLRs (20, 24–28).

1.1.3 The ROQ1-XopQ complex as a model for studying TNLs and direct effector recognition

Recognition of XopQ 1 (ROQ1) is a plant TIR-NLR resistance gene native to the tobacco species *Nicotiana benthamiana*. ROQ1 is able to recognize the XopQ effector from *Xanthomonas*, HopQ1 from *Pseudomonas* (29) and RIPB from *Ralstonia solanacearum* (30). Recognition of XopQ by ROQ1 triggers ROQ1 oligomerization and downstream ETI signal transduction, leading to a hypersensitive cell death response resistance and resistance to pathogen invasion in an EDS1-dependent manner (20, 29, 31). To further our understanding of the molecular events that control the direct recognition of pathogen effectors by TNL immune receptors, we employed cryo-EM to solve the structure of the ROQ1-XopQ complex purified directly from *Nicotiana benthamiana* leaves.

1.2 Results and discussion

1.2.1 Insights from the ROQ1-XopQ complex purification

XopQ recognition by ROQ1 triggers a rapid cell death response in wild type *N. benthamiana* leaves, making it difficult to obtain sufficient protein for expression and

purification (29). All plant TNLs require the downstream EDS1 protein to achieve cell death and express disease resistance (25). In order to obtain live tissue for protein purification, we transiently co-expressed ROQ1 and XopQ by *Agrobacterium*-mediated transformation in CRISPR-induced *eds1-1* mutants of *N. benthamiana* known to prevent ROQ1-induced cell death (20).

Our initial attempt to purify the ROQ1-XopQ complex was inspired by Tenthoirey et al. 2017, in which they purified the NAIP5-NLRC4 complex by flag-immunoprecipitation (flag-IP) followed by size exclusion chromatography (32). Previous studies had already shown that ROQ1-3xFlag co-precipitated with XopQ by flag-IP (20). In our first successful pilot experiment, we purified the ROQ1-XopQ complex from 10 grams of leaf extract using a flag pulldown followed by size exclusion chromatography. This purification yielded enough protein to detect by western blotting but not enough to solve its structure by cryo-EM. In further purification attempts we tried using more leaf tissue, different ways of concentrating the proteins and trying different affinity tags (Fig. 1). During this process, we learned to avoid steps that require centrifugal filters, as they caused the complex to precipitate, and the use of low specificity affinity resins, such as Ni-NTA. We also improved sample yield by adding a secondary cell lysis step to our protocol. Once the leaf material was finely ground using a pestle and mortar, we resuspended the powder in buffer and sonicated it to further break up the cells.

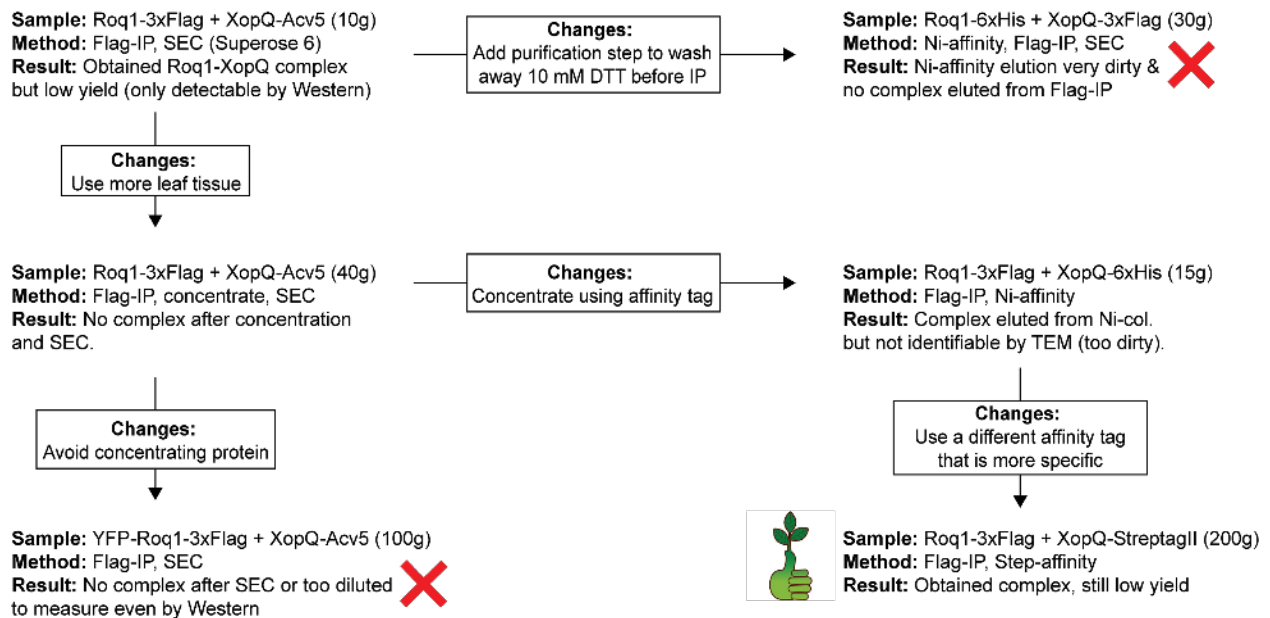


Figure 1.1 Purification trials leading to our successful protocol.

Ultimately, we successfully purified the ROQ1-XopQ complex by first capturing the sample from the cell lysate by flag-IP and subsequently purifying it with a strep pull down, in which we eluted the sample in a small volume to concentrate the sample. We chose not to purify the sample further by size exclusion chromatography because we

did not want our particles to become too diluted. This purification yielded enough protein to detect via silver staining, which has a sensitivity limit of 2 ng (Fig. 1.2).

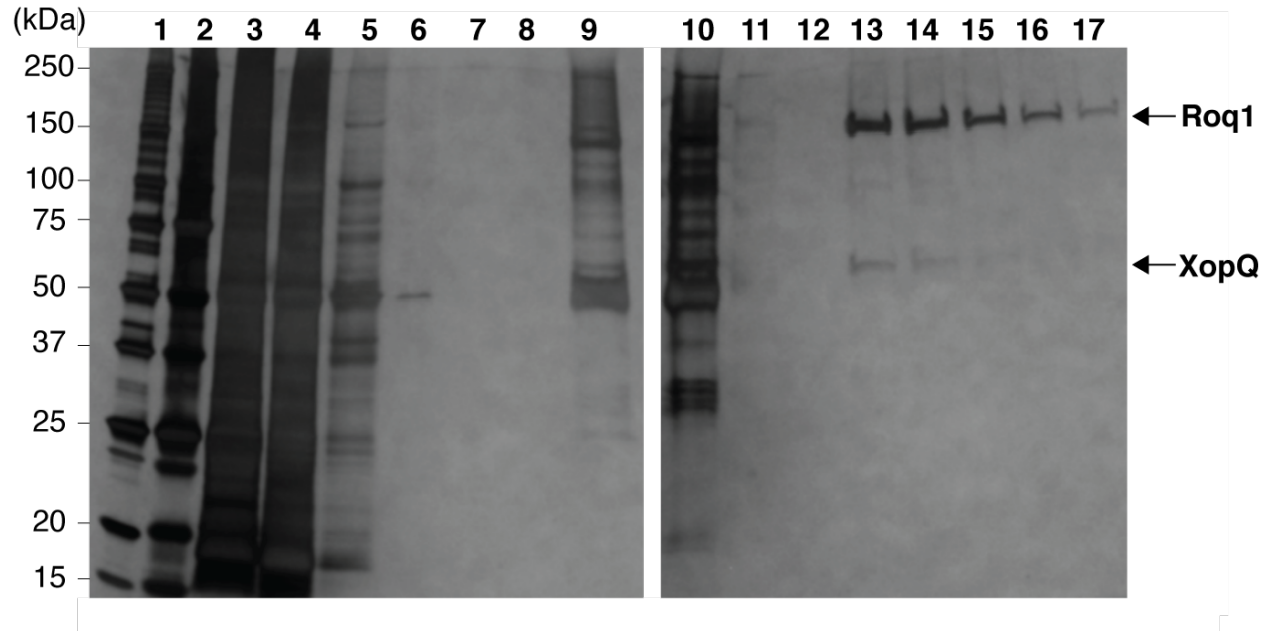


Figure 1.2 Steps in the purification of the ROQ1-XopQ complex visualized by silver stained SDS-PAGE. Lane are numbered as follows: **1:** 0.5 µL Ladder (Bio-Rad Precision Plus Protein Unstained Standards). **2:** 2.5 µL Ladder. **3:** Lysed cells. **4:** Flowthrough after binding Roq1-Flag to ANTI-FLAG M2 affinity gel (Sigma-Aldrich). **5-8:** Successive washes of ANTI-FLAG M2 affinity gel. **9:** Elution from ANTI-FLAG M2 affinity gel **10:** Flowthrough after binding StrepII-XopQ to Strep-Tactin Superflow Plus resin (Qiagen). **11-12:** Successive washes of Strep-Tactin Superflow Plus resin. **13-17:** Successive elutions from Strep-Tactin Superflow Plus resin (10 µL loaded).

1.2.2 Insights from the cryo-EM sample preparation, data collection and processing

The concentration of purified ROQ1-XopQ complex was too low to solve the structure using standard methods. In order to accumulate enough particles onto the cryo-EM grid, we used a thin layer of amorphous carbon that was floated on top of a holey-carbon copper grid as a support for our particles to bind to. In a typical experiment, incubating 4 µL of sample at a 20 nM concentration for 5 minutes is enough to cover a carbon-coated grid with particles. Yet, the concentration of the ROQ1-XopQ complex was still too low to obtain enough particles using this method. In order to improve the particle count, we increase the sample incubation to 90 min inside a teflon well (Fig. 1.3). This lowered the surface area of the air-water interface, thereby protecting the complex during a long incubation period, and allowing us to make multiple grids using the same 20 µL of purified sample.

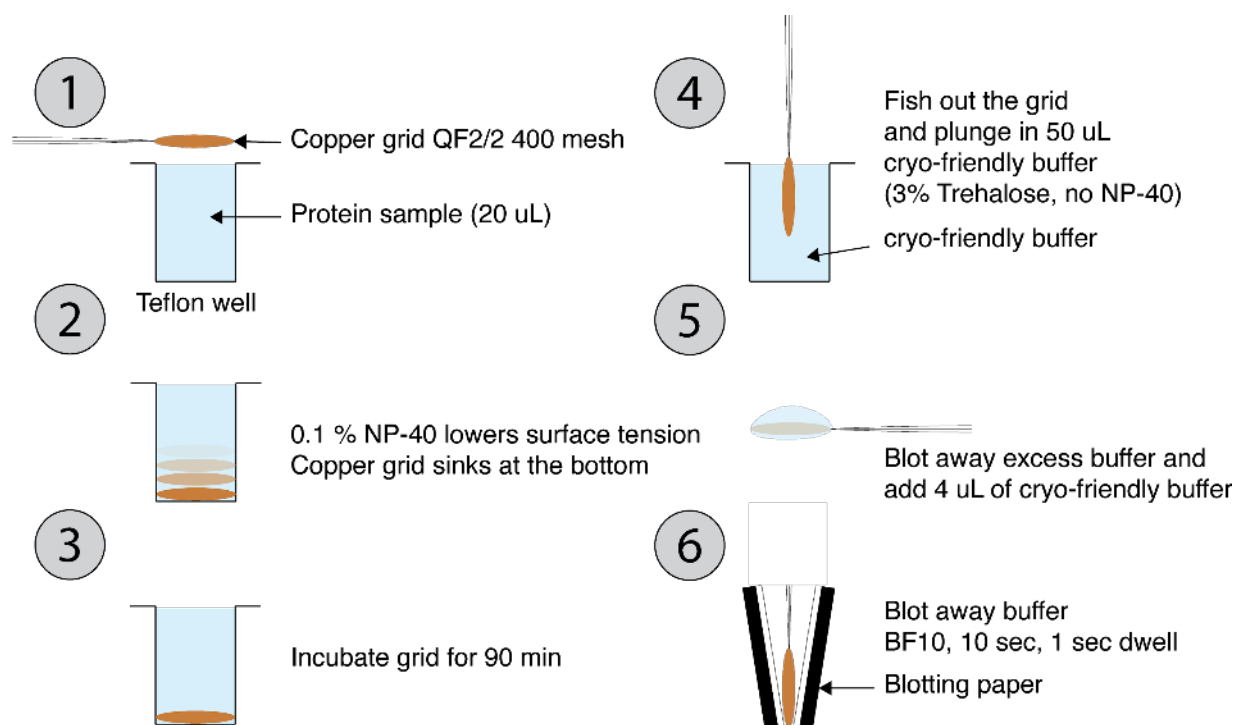


Figure 1.3 Sample application onto a cryo-EM grid coated with a layer of amorphous carbon.

Being limited by sample amount, it was essential for this study that we maximize the amount of data that could be collected on the electron microscope. To this end, we prepared our sample on a holey-carbon grid with a large hole size (2 μm) and collected our data on a Titan Krios, which has a 3-condenser lens system. This feature allows the formation of a smaller parallel beam than on 2-condenser instruments such as the Talos Arctica, and enables the acquisition of multiple exposures per hole (33). In our case, 4 micrographs were collected per hole. The speed of our data collection was also improved using beam-shift acquisition, enabling us to collect data from 5 holes per stage drift.

The disc shape of the ROQ1-XopQ complex lends it to favorably deposit on the grid on its flat surface, making side views of the particles rare. Finding rare views was also complicated by the high number of contaminants, such as protein aggregates and ice. Rare views can easily be lost by converging into poor quality classes during a 2D classification, therefore we chose to initially sort our particles by 3D classification. This method has been shown to capture rare views in other cryo-EM studies (34, 35). Once the majority of our contaminants were filtered out of our dataset, we captured the rare side views with multiple rounds of 3D refinement and alignment-free 3D classification until we obtained a class in which both top and side views converged.

1.2.3 The overall structure of the ROQ1-XopQ complex

Cryo-EM imaging and analysis of the affinity-purified complex yielded a reconstruction at 3.8 \AA overall resolution with C4 symmetry imposed (Fig. 1.5) and showed that the ROQ1 protomers assemble into a tetrameric, four-leaf clover structure with XopQ present in a 1:1 ratio (Fig. 1.4). We find that the NBD (Nucleotide-Binding

Domain), HD1 (Helical Domain 1), and WHD (Winged Helix Domain) provide the necessary contacts for ROQ1 oligomerization and bring together the four TIR domains. The LRR features the characteristic horseshoe shape and wraps around the XopQ effector protein, recognizing its surface residues. The cryo-EM map also reveals a previously uncharacterized Post-LRR (PL) domain at the C-terminal end of the LRR connected by a short ten residue linker. The XopQ effector is in its open conformation, exposing the cleft of the predicted nucleoside hydrolase active site. XopQ's specific substrate remains unidentified, but previous studies have shown that XopQ binds ADPR, an important immune signaling molecule in plants, consistent with its immunosuppressive function (36). In the following chapters, we discuss the structural features describing ROQ1 substrate recognition (Chapter 2), oligomerization of ROQ1 (Chapter 3), and TIR domain association (Chapter 4).

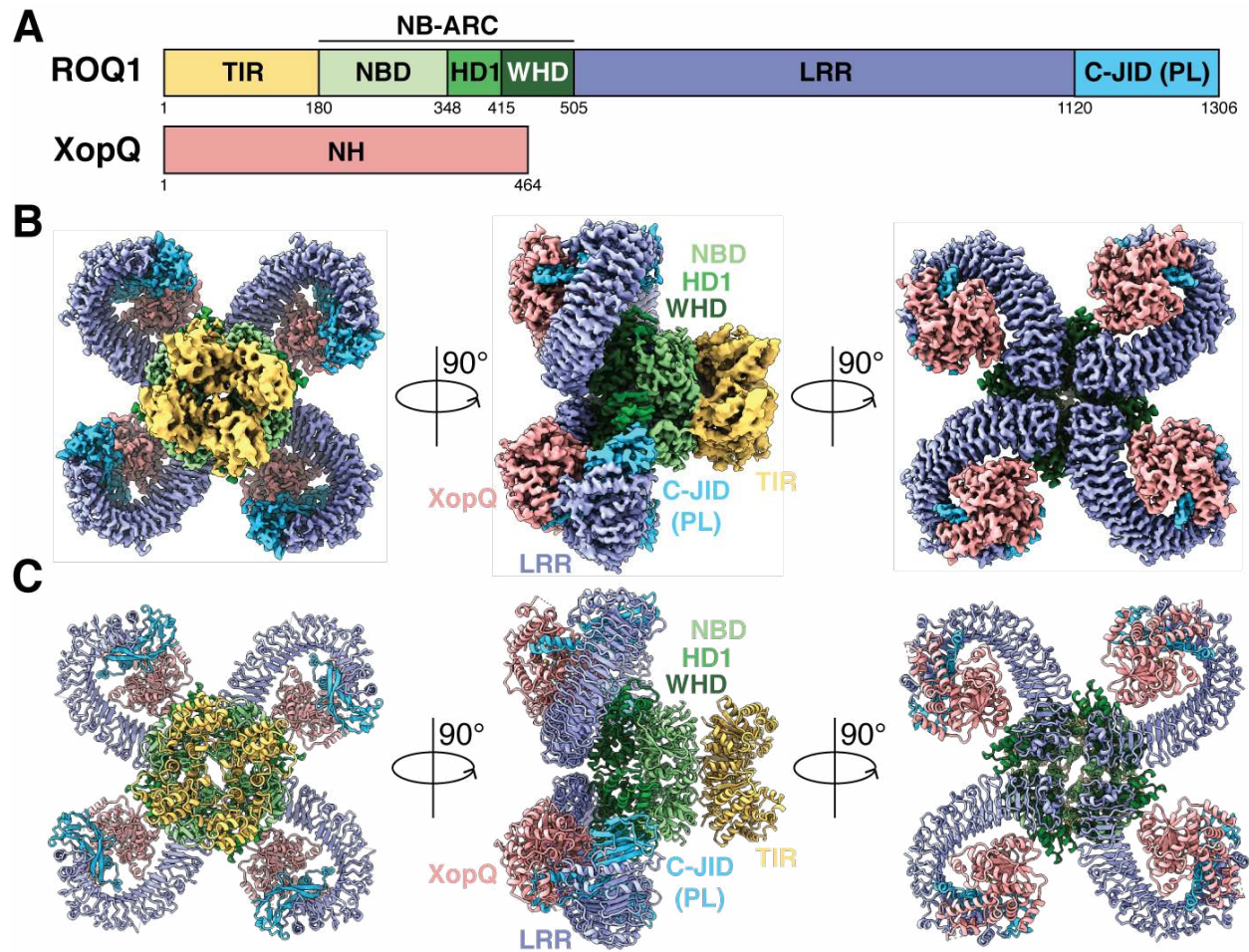


Figure 1.4 Overall structure of the ROQ1-XopQ complex. (A) Schematic representations of ROQ1 and XopQ with color-coded domain architecture: TIR (yellow), NB-ARC (NBD-HD1-WHD) (light green, green, dark green respectively), LRR (violet), C-JID (or PL domain) (light blue), and XopQ (salmon). (B) Composite density map of the ROQ1-XopQ complex from three cryo-EM reconstructions and corresponding atomic model (C), shown in three orthogonal views. Colors according to the nomenclature in (A).

1.3 Conclusion

Structural studies of NLRs and their mechanism of action have been hampered by their low levels in native tissue, our inability to express them recombinantly, and their instability in solution. Through repeated attempts to purify the ROQ1-XopQ complex we designed a protocol that yielded enough sample to pursue solving its structure by cryo-EM. Additional optimization in cryo-EM grid preparation was also required to maximize the amount of particles. Together, our methods enabled us to overcome sample limitation problems and solve a 3.8 Å resolution cryo-EM structure of the NLR Roq1, bound to the pathogenic effector protein XopQ, directly extracted from agro-infiltrated *Nicotiana benthamiana* leaves.

1.4 Material and Methods

1.4.1 Plant Materials and Growth Conditions

The *N. benthamiana* *eds1-1* mutant was described as previously (14). The binary vector containing ROQ1 guide sequence (GATGATAAGGAGTTAAAGAG) and Cas9 was described previously (15) was transformed into agrobacterium and used for generating *N. tabacum* ROQ1-1 stable mutant plants by CRISPR-Cas9 gene editing system. *N. benthamiana* and *N. tabacum* plants were grown in a growth chamber under a 8-hr-light/16-hr-dark photoperiod at 23-25°C.

1.4.2 Expression and purification of the ROQ1-XopQ complex

ROQ1 and XopQ were fused with C-terminal 3xFlag tag and N-terminal StrepII tag, respectively, and transformed into Agrobacterium GV3101. The agrobacterium GV3101 strains containing ROQ1-3xFlag and StrepII-XopQ were co-inoculated into *N. benthamiana* *eds1-1* mutant leaves. At 30 hours after infiltration, 200g of leaves were harvested and ground using a mortar and pestle and resuspended in 400 mL of Lysis Buffer (50 mM HEPES pH 7.5, 1 mM EDTA, 5 mM MgCl₂, 150 mM NaCl, 10 mM KCl, 0.4% NP40, 5% glycerol, 10 mM DTT) supplemented with protease inhibitors (100 uM PMSF, 1 uM Phosphoramidon, 10 uM 1,10-Phenanthroline, 1uM Pepstatin A, 10 uM Leupeptin, 2 uM E-64, 10 uM Bestatin and 2 ug/mL Aprotinin). Leaves were further lysed by sonication for 2 min at 20 kHz. The cell lysate was initially centrifuged at 18,000xg for 45 min to pellet large debris and the harvested supernatant was further centrifuged at 40,000xg for 45 min to remove any smaller residuals. The clarified extract was then incubated with 800 μ L (bed volume) of ANTI-FLAG M2 affinity gel (Sigma-Aldrich) for 3 hours at 4°C. The gel was washed with 10 CV of Wash Buffer (20 mM HEPES pH 7.5, 1mM EDTA, 5 mM MgCl₂, 150 mM NaCl, 10 mM KCl, 0.2% NP-40, 10% glycerol) and the sample was eluted twice by incubating in 1 CV of Wash Buffer supplemented with 300 μ g/mL of 3xFlag peptide for 30 min. Each wash and elution was separated from the affinity-resin by centrifugation at 300xg for 5 min. Eluates were pooled and incubated with 20 μ L (bed volume) of Strep-Tactin Superflow Plus (Qiagen) resin for 1 hour. The resin was then washed with 10 CV of Wash Buffer and the totality of the sample was eluted in 5 sequential steps by adding 1 CV Wash Buffer supplemented with 10 mM Biotin. Each wash and elution was separated from the affinity-resin by centrifugation at 300xg for 5 min. The protein complex was flash frozen in liquid N₂ and stored at -80°C. We were unable to accurately measure the final protein concentration due to low amounts of sample.

1.4.3 Sample Preparation for Cryo-EM

QUANTIFOIL R2/2 holey carbon grids were coated with a thin film of continuous carbon (approximately 3 nm thick) and plasma cleaned (Tergeo-EM, PIE Scientific LLC, operating at 15 W for 30 sec in indirect mode) before addition of sample. Because of the low concentration of the ROQ1-XopQ complex in our sample, we attempted to float the carbon-coated grid on the sample drop to enable prolonged incubation to allow attachment of more molecules to the carbon. However, due to the high detergent concentration of the sample buffer, loss of surface tension caused the grids to sink to the

bottom of the drop. Therefore, we used a Teflon well to hold 20 μL of sample (supplemented with 1 mM ATP) and deposited the grid in the well carbon side up, upon which the grid fell to the bottom of the well, allowing sample adsorption to the carbon-coated side. The grid was incubated with the sample for 90 min at 4°C. It was then removed from the drop and washed in a 50 μL drop of cryo-EM-friendly buffer (10 mM HEPES pH 7.5, 1 mM EDTA, 5 mM MgCl_2 , 150 mM NaCl, 10 mM KCl, 3% trehalose). We gently blotted the grid using filter paper and added 4 μL of cryo-EM-friendly Buffer before mounting the grid onto a Thermo Fisher Scientific Vitrobot Mk. IV set to 100% humidity, cooled to 4°C and loaded with Whatman Grade 1 Qualitative Filter Paper (GE Healthcare). The grid was immediately blotted for 10 sec (blot force 10) and plunge-frozen in liquid ethane.

1.4.4 Data Collection

The grid was loaded onto a Titan Krios cryo-electron microscope (Thermo Fisher Scientific) operating at 300 kV and equipped with a K3 direct electron detector camera (Gatan) mounted behind a BioQuantum energy filter (Gatan). Electron micrographs were acquired as dose-fractionated movies (11,134 movies in total) in super-resolution counting mode with the microscope set to 80,879x magnification (corresponding to a pixel size of 0.9386 Å) and a total electron exposure of 50 $\text{e}^-/\text{Å}^2$. Defocus values ranged from -0.9 to -2.5 μm . Automated data collection was controlled by SerialEM. For high-throughput data collection, we used image shift with active beam tilt correction enabled to collect 20 movies at each stage position. All other parameters can be found in Table S1.

1.4.5 Data Processing

All processing steps were performed using RELION 3.1 (37) unless otherwise indicated. Movies were imported into RELION and classified into 5 optics groups according to the respective beam shift used during acquisition. Alignment of the movie frames was performed using MotionCor2 (38) and GCTF (39) was used for fitting of the contrast transfer function and defocus estimation. To ensure that we captured particles in all poses present on the grid, we used the unbiased Laplacian-of-Gaussian autopicker (40) in RELION for particle picking. Instead of 2D classification, an initial 3D classification (with C4 symmetry applied) was performed in order to prevent loss of rare views that might be classified into classes containing broken particles or false-positive particle picks in 2D classification. An initial reconstruction of the ROQ1-XopQ complex generated in cryoSPARC (41) from a grid quality screening session was used as the reference model. The particles from the best classes in this initial 3D classification were subjected to successive rounds of alignment-free 3D classification, and alignment-free 2D classification for each 3D class, followed by removal of bad particles and 3D refinement. This enabled us to recover the side views of the ROQ1-XopQ complex, which we failed to do using alternative processing approaches. A final round of 3D-refinement and alignment-free 3D classification ($\tau = 16$) yielded one high-quality class containing 15,263 particles, with a broad distribution of projection directions. After CTF-refinement and Bayesian polishing (40) of these particles, 3D-refinement resulted in a reconstruction of the ROQ1-XopQ complex at 3.8 Å resolution overall (FSC = 0.143). This initial map

was of sufficient quality for atomic model building of the NB-ARC region (NBD-HD1-WHD) as well as the most N-terminal portion of the LRR. Further processing was needed to improve the LRR-PL-XopQ and TIR domain regions, as described in the next chapters.

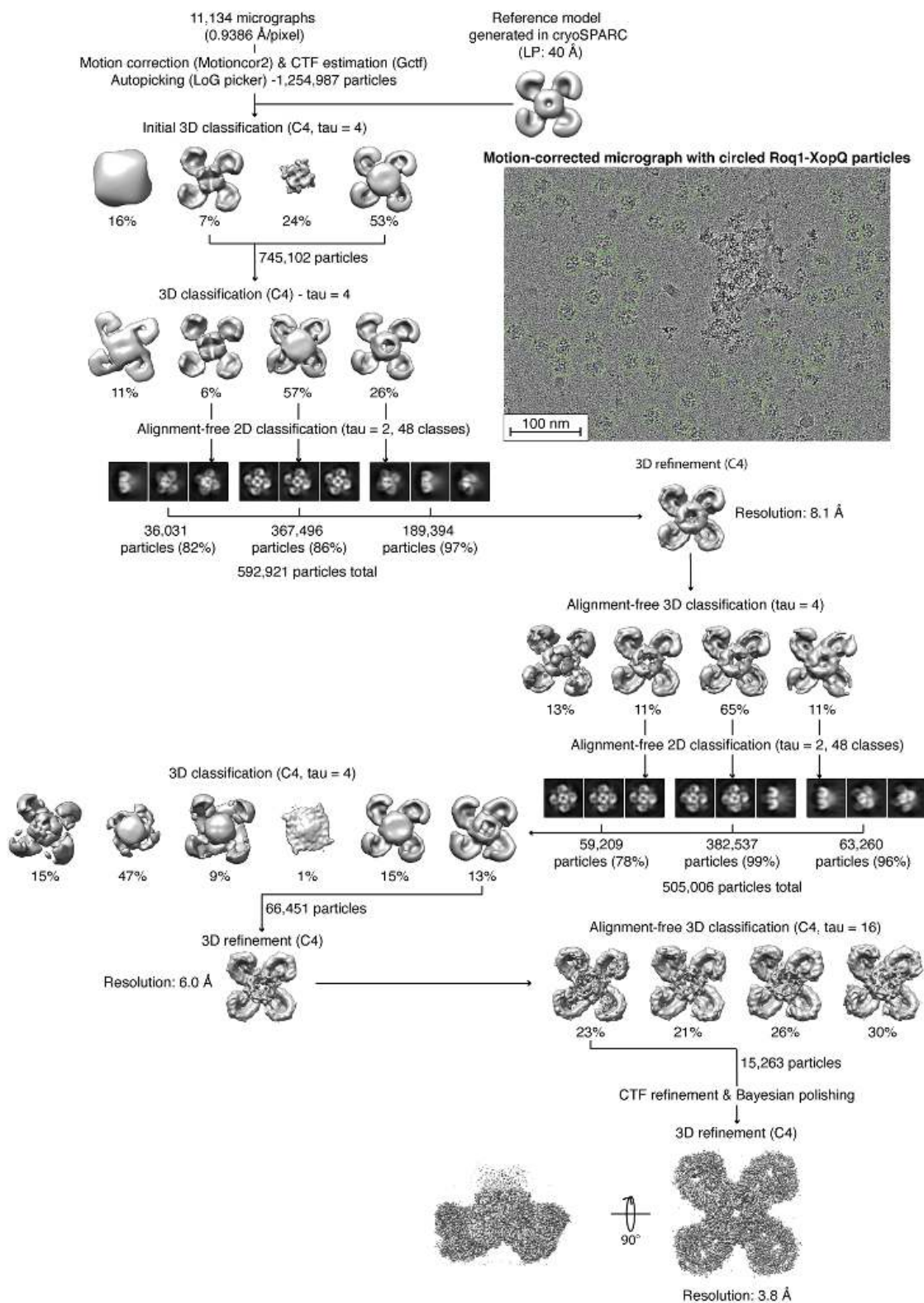


Figure 1.5 Cryo-EM data processing tree from collected EM movies to the initial reconstruction of the ROQ1-XopQ complex.

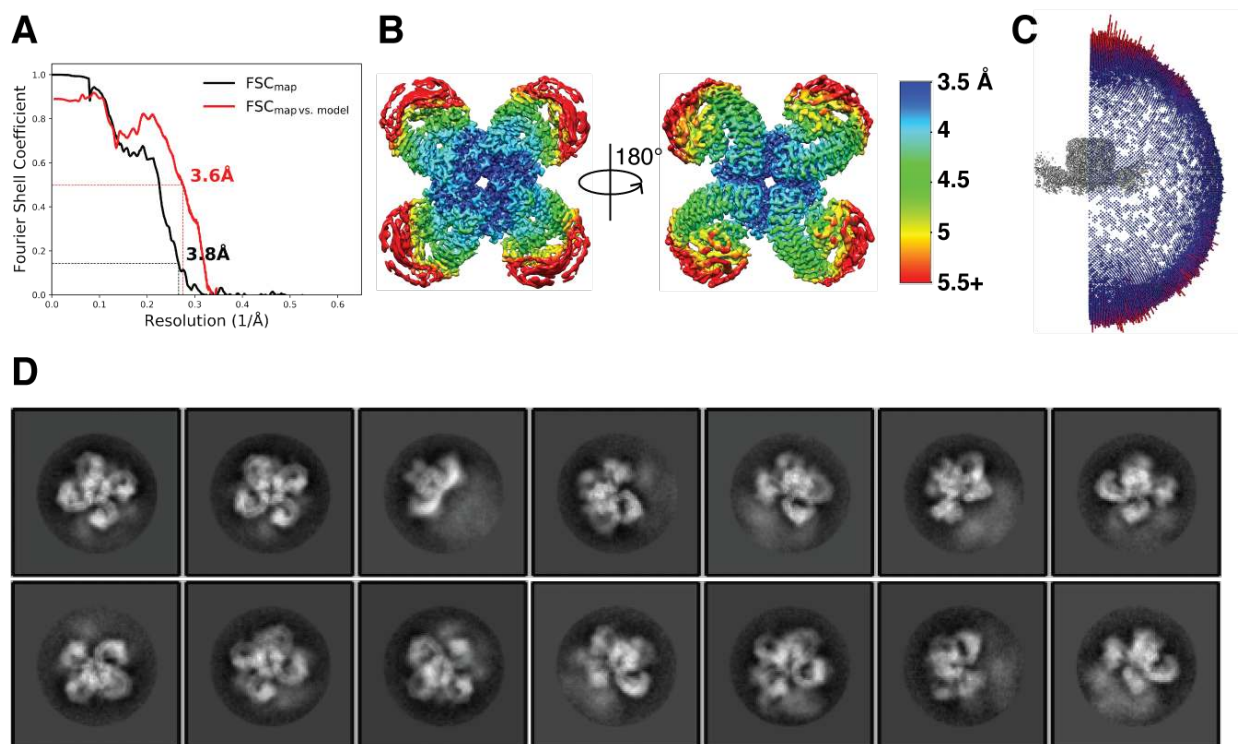


Figure 1.6 Resolution estimation. (A) map FSC and map vs model FSC. (B) Cryo-EM density color-coded according to local resolution. (C) Angular distribution plots of particles included in the 3D reconstruction. (D) 2D classification of the particles included in the initial reconstruction.

1.4.5 Model Building and Refinement

A model generated using SWISS-MODEL (42) based on the structure of ZAR1 NBD (PDB: 6J5T) was docked into our cryo-EM map using UCSF Chimera (61). This model served as a starting point to build the structure of the NB-ARC domain manually in COOT (43). Our initial map of the ROQ1-XopQ complex was used to build residues 189-625 of ROQ1 as well as for fitting the ATP ligand. The atomic model of the NB-ARC domain was refined with successive rounds of real-space refinement in PHENIX (44). Iterative rounds of rigid-body refinement, morphing and gradient driven global minimization were used in the initial stages of refinement while applying ramachandran, rotamer, C_β , and secondary structure restraints throughout to maintain good model geometry at the resolution of our cryo-EM maps. Internal symmetry (C_4) was imposed on the NB-ARC model. Structural issues were corrected manually in COOT (43) between rounds of refinement. The final model was refined using atomic displacement parameter refinement and gradient driven global minimization while applying the same restraint as described previously. The model was validated using MOLPROBITY (45) within PHENIX (44), and the model vs. map FSC was calculated using the MTRIAGE (46) validation tool in PHENIX (44).

1.4.6 HR phenotype and co-immunoprecipitation

The various ROQ1 mutants were made and constructed into PE1776 vectors fusing with a C-terminal 3Flag tag. For HR phenotype observation, ROQ1 mutants and StrepII-XopQ were transiently co-expressed in *N. tabacum roq1-1* mutant leaves via agrobacterium mediated transformation. HR phenotypes were observed and imaged 2 days post infiltration. To detect protein expressions, ROQ1 mutants and StrepII-XopQ were co-expressed in *N. benthamiana eds1-1* mutant leaves, extracted using protein extraction buffer (50 mM Tris-HCl, pH 7.5, 150 mM NaCl, 1mM EDTA, 0.2% Nonidet P-40, 0.2% Triton X-100, 6 mM β -mercaptoethanol, 10mM DTT and 1 \times Protease Inhibitor Cocktail), boiled in Laemmli buffer for 5 min and separated on 8% SDS-PAGE gels. StrepII-XopQ were detected with the primary StrepTag II monoclonal antibody (A02230, Abbkine) and the second antibody (A4416, Sigma). ROQ1 mutants were enriched by ANTI-FLAG M2 Affinity Gel (A2220, Sigma-Aldrich) before boiled, and detected with the primary monoclonal anti-Flag antibody (F1804, Sigma-Aldrich) and the second antibody (A4416, Sigma).

1.4.7 Data Deposition

The cryo-EM maps have been deposited in the Electron Microscopy Data Bank (EMDB) and the refined atomic models have been deposited in the Protein Data Bank (PDB). Accession codes are listed in table Supplemental Table 1.1.

Data Collection

Microscope	Krios
Voltage (kV)	300
Detector	K3
Magnification	80,879x
Energy filter slit (eV)	25
Movies	11,134
Pixel size (Å)	0.9386
Defocus range (μm)	-0.9 to -2.5
Exposure (e ⁻ /Å ²)	50
Exposure rate (e ⁻ /Å ² /frame)	1
Automation software	SerialEM

Reconstruction

Region	Initial reconstruction	LRR-PL-XopQ	TIR domains
Software	RELION	RELION	RELION
Particles (initial)	1,254,987	1,254,987	1,254,987
Particles (final)	15,263	15,263	5,466
Box size (pixels)	480	480	480
Accuracy rotations (°)	0.84	1.28	1.94
Accuracy translations (Å)	0.63	0.98	1.2
Map resolution (Å) FSC = 0.143/0.5	3.8/4.4	3.8/4.4	4.6/8.3
Map sharpening B-factor (Å ²)	-82	-67	-97
Local resolution range (Å)	3.4-9.3	3.8-9.7	5.3-24.6

Coordinate Refinement

Software	PHENIX	PHENIX	PHENIX
Resolution Cutoff	3.6	3.8	6
FSC model vs. map = 0.5 (Å)	3.6	3.9	7.7
Model vs. map CC (global/local)	0.80/0.82	0.78/0.78	0.44/0.43

Model

Number of residues

Protein	1748	1079	664
Ligands	8 (4 ATP & 4 Mg ²⁺)	1 (Ca ²⁺)	None

B-factor (Å²)

Protein	39	65	194
Ligand	31	47	N/A

R.m.s deviations

Bonds lengths (Å)	0.003	0.003	0.001
Bond angles (°)	0.74	0.772	0.417

Validation

Molprobity score	1.97	2.11	1.52
Molprobity clashscore	9.27	11.55	2.96
Rotamer outliers (%)	0	0.21	0
C _β deviations (%)	0	0	0

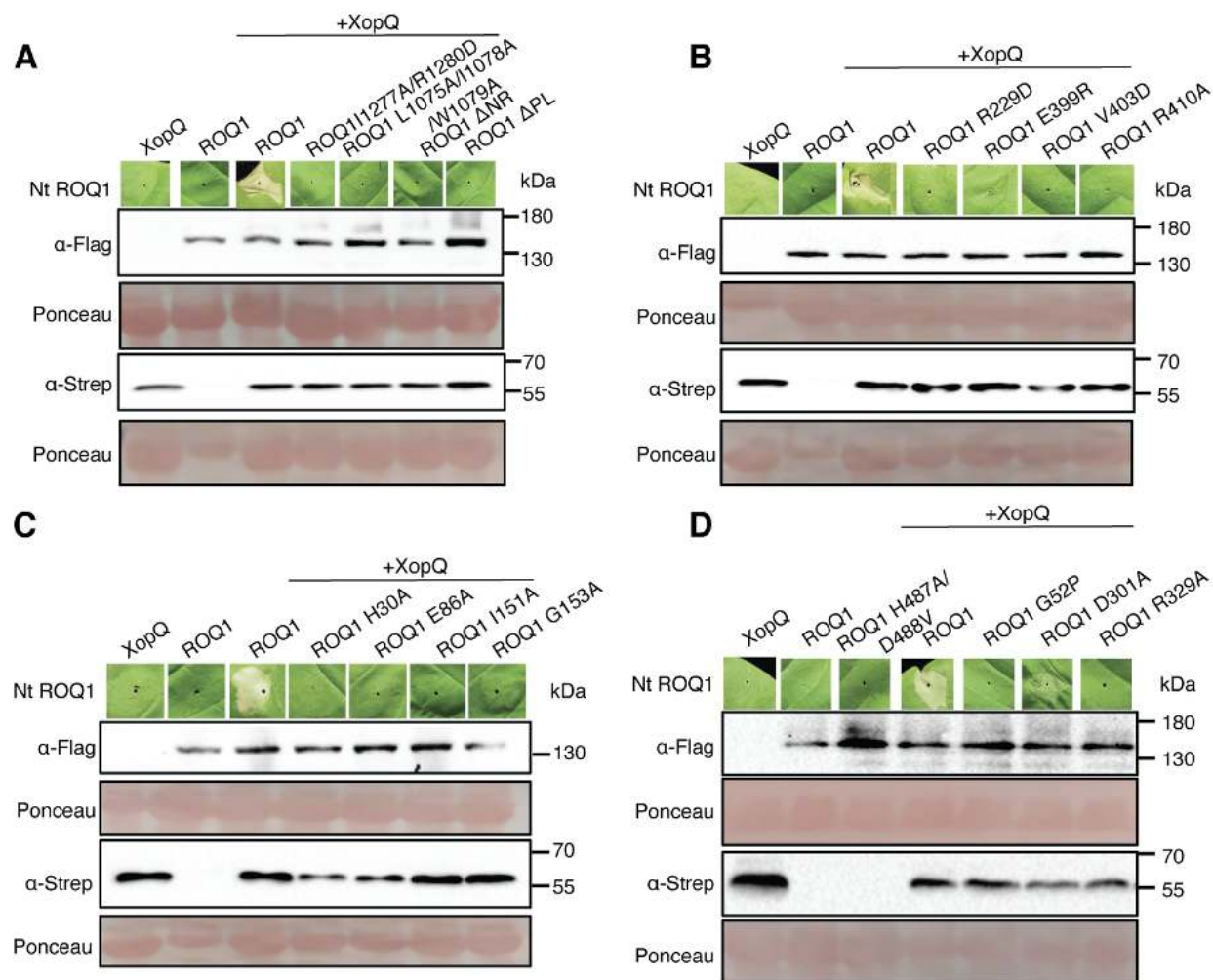
Ramachandran plot

Favored (%)	92.18	90.72	93.29
Allowed (%)	7.82	9.28	6.71
Outliers (%)	0	0	0
CaBLAM outliers (%)	7.16	5.69	2.47
EM ringer score	1.74	1.46	N/A (C _α only)

Deposition

PDB	7JLV	7JLU	7JLX
EMDB	22381	22380	22383

Supplemental Table 1.1 Data collection, 3D reconstruction, and refinement statistics.



Supplementary Figure 1.1 HR Phenotype and Protein Expression of ROQ1 mutants. The HR phenotype is detected on the leaf tissue at the site of agrobacterium injection (top row). Expression of ROQ1 and XopQ was detected by Western-blotting using an anti-Flag antibody and an anti-StrepTagII antibody respectively. Ponceau staining was used for the detection of protein bands on the Western-blot. (A) Mutation in the LRR-PL-XopQ interface. Residues providing contacts between XopQ and the LRR (ROQ1 L1075A/I1078A/W1079A) as well between XopQ and the PL domain (ROQ1 I1277A/ R1280D, ΔNR and ΔPL) were mutated. For the ΔNR mutant, residues corresponding to the NR loop of Roq1 (1163-1195) were replaced with a flexible linker with the following sequence: SGGGSGGS. For the ΔPL mutant, the C-terminal end of ROQ1 (1129-1306), corresponding to the PL domain, was truncated. (B) Mutations at the oligomerization interface of ROQ1 in the NB-ARC domain. More specifically, the R229 is at the NDB-NBD interface and E399, V403 and R410 are at the HD1-WHD interface. (C) Mutations in the TIR domain of ROQ1 at the AE (H30A) and BE (I151A, G153A) interfaces. The catalytic glutamate in the active site of the TIR domain (E86) was mutated to an alanine. (D) Additional mutations: in the MHD motif (H487A/D488V), the TIR domain BB-loop glycine (G52P), the Walker B motif (D301A) and the TTR motif (R329A).

Chapter Two

Recognition of the pathogen effector XopQ by ROQ1

Note: These results have been published and are discussed in more detail in our recent paper Martin et al. 2020 (1).

2.1 Introduction

NLRs can sense pathogen invasion directly through physical interaction with effectors or indirectly by monitoring the biochemical status of a guard or decoy protein that is associated with the NLR (9, 47). The LRR is thought to serve as the substrate recognition platform for effector, guard or decoy proteins involved in NLR activation. Additional domains have also been found to play a critical role in substrate recognition. For example, many NLRs contain an Integrated Domain (ID), typically at the C-terminal end, that serves to bind the effector (3). In other cases, domains that play a role in NLR oligomerization, such as HD1 and HD2 in NAIP5, also participate in substrate recognition (32). Here, we provide a structural basis for direct effector binding by the LRR and PL domain of ROQ1 to recognize the XopQ.

2.2 Results & Discussion

2.2.1 Substrate recognition by the LRR

The 24 leucine-rich repeats of ROQ1 form a 150 Å long scaffold that bends around XopQ, displaying key contact residues along its surface (Fig. 2.1). We find the LRR of ROQ1 interacts with the effector in two different ways: (i) In the region where XopQ is in close contact with the LRR scaffold, several side chains exposed on the surface of the LRR directly interact with the substrate (Figure 2.1A). A similar mechanism is utilized by the LRRs of the CC-NLR ZAR1 to recognize RKS1 and TLR3 to recognize dsRNA (11, 48). The majority of these residues have large aromatic side chains that recognize hydrophobic patches and grooves on the surface of XopQ; (ii) In regions where the LRR scaffold is too far away to interact with the effector directly, we find an elongated linker between two leucine-rich repeats (LRRs 23 and 24) that reaches over to bind XopQ (Figure 2.1B). A small amphipathic α -helix is formed at the site of contact, with hydrophobic side chains recognizing conserved residues at the outer edge of XopQ's active site cleft (Y311^{XopQ}, H433^{XopQ}) (Figure 2.1B). The extended linker then loops back towards the scaffold and forms the next repeat in the LRR. Mutating the residues that form the hydrophobic face of the α -helix (L1075^{ROQ1}, W1079^{ROQ1}, I1078^{ROQ1}) to alanines resulted in loss of the HR phenotype, suggesting these interactions are critical for XopQ recognition (Supplementary Fig. 1A).

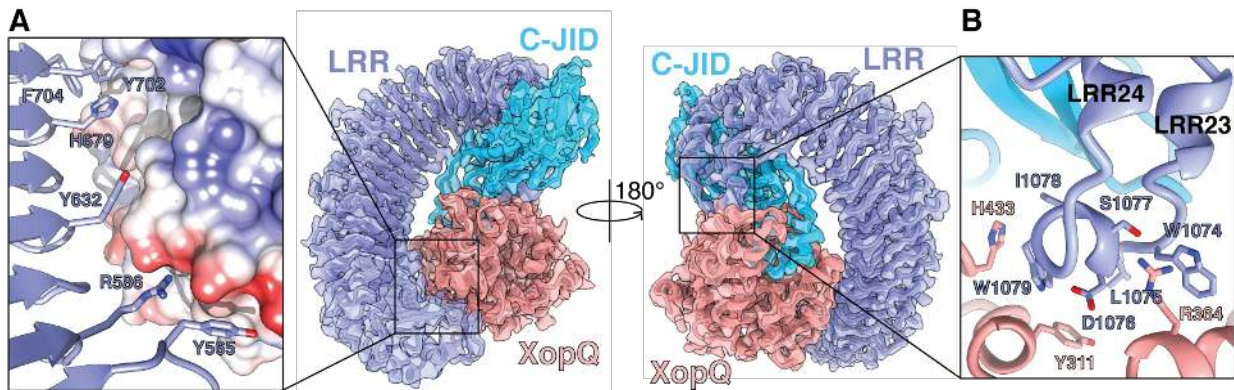


Figure 2.1 Structure of the ROQ1 LRR binding to XopQ. (A) Surface contacts between the N-terminal region of the LRR, shown with violet ribbon and XopQ represented by its Coulombic surface potential. (B) The elongated LRR between repeats 23 and 24 (violet) interacting with XopQ (salmon).

2.2.2 Characterization of the Post-LRR domain

A 10-residue linker (aa. 1120-1129) connects the C-terminal end of the LRR to the PL domain, which also interacts with XopQ. This domain folds into a β -sandwich, with 9 antiparallel β -strands arranged into two β -sheets (Fig. 2.2, 2.3). The last LRR forms hydrogen bonds with one of the β -strands, thereby rigidifying the conformation between the two domains (Fig. 2.3A,B). Because PLs serving in pathogen detection have been found in other TNLs, but remain poorly characterized, we sought to further investigate possible structural homology of the ROQ1 PL domain with published structures (49). Analysis using the CATH database (50) revealed proteins with immunoglobulin-like and jelly-roll folds as the closest structural homologues (Fig. 2.2A). Furthermore, the PL domain of RPP1, another TNL, shares a similar structure to the PL domain in ROQ1 (51) despite having poor sequence identity (14.29%) (Fig. 2.2A,C). The core of this domain in RPP1 also folds into a β -sandwich structure that forms hydrogen bonds with the last β -strand of the LRR (51). Both share the same β -strand topology with the exception of a ninth C-terminal β -strand present in ROQ1 (Fig. 2.2B). The major structural differences in the ROQ1 and RPP1 PL domain are found in the loops that interconnect the β -strands and serve to recognize their respective substrates. Domains fused to the C-terminus of LRRs are found in many other NLRs (3, 49) and are likely to differ in structure and function. Therefore, to address the specific type of PL domain utilised by ROQ1 and RPP1, we refer to it as the C-terminal Jelly-roll/Ig-like Domain (C-JID).

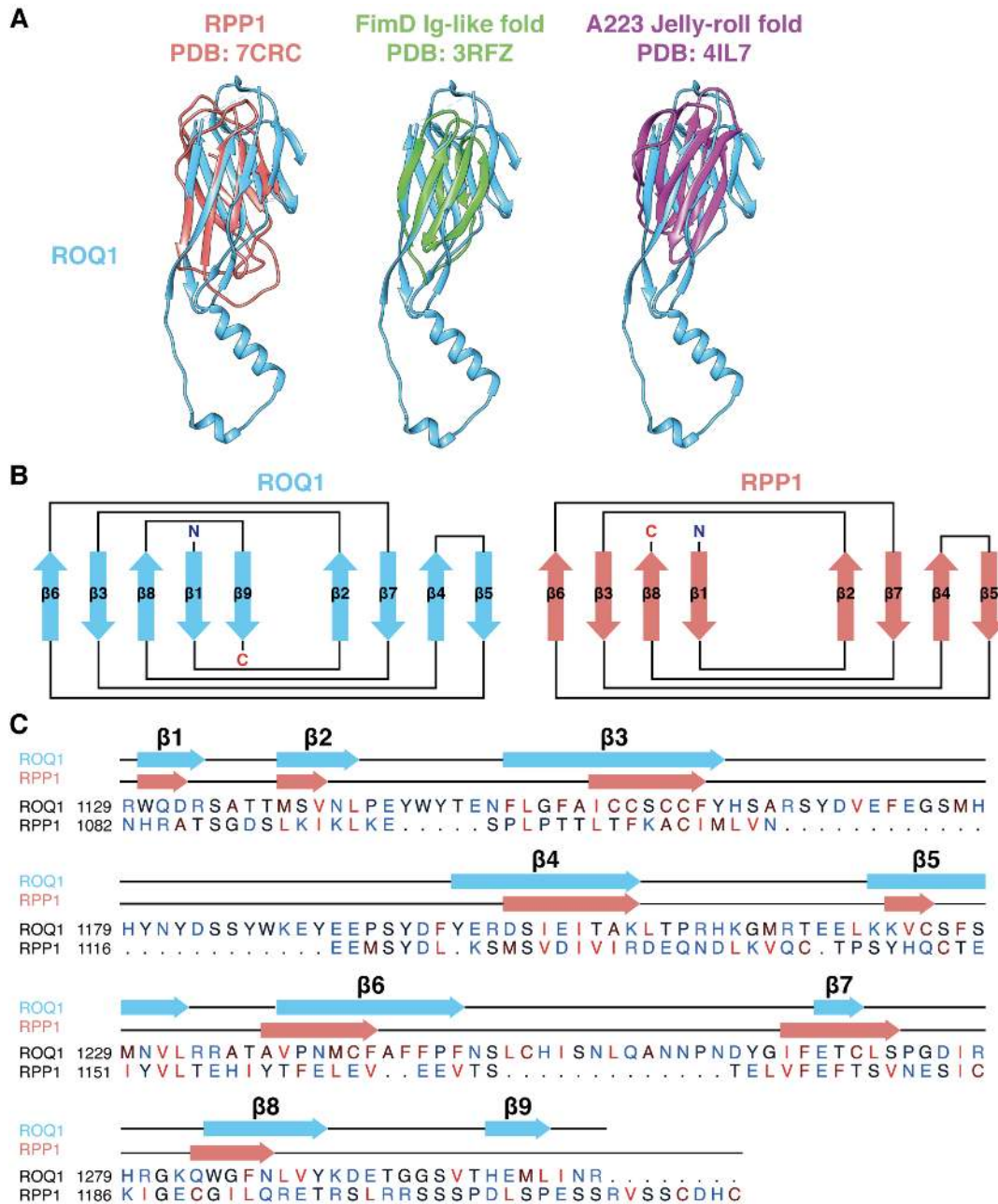


Figure 2.2 Comparison between the ROQ1 C-JID (PL domain) and the RPP1 C-JID. (A) From left to right: Structural alignment of the ROQ1 C-JID with the RPP1 C-JID (PDB: 7CRC), the Ig-like fold in FimD (PDB: 3RFZ), and the Jelly-roll fold in A223 (PDB: 4IL7). FimD and A223 were among the highest scoring structural homologues of the ROQ1 C-JID found using the CATH database and were used as representatives of their respective folds. (B) β -strand topology of ROQ1 (left) and RPP1 (right). The only difference found is at the 9th β -strand of ROQ1 which does not appear in the RPP1 structure. (C) Local sequence alignment between the ROQ1 C-JID (1129-1306) and the RPP1 C-JID (1082-1221). Positions of the β -stands in ROQ1 and RPP1 are labeled along the sequence using the same color code as in panel B. Residues are colored according to the Kyte-Doolittle hydrophobicity scale, with polar residues colored in blue, intermediate residues in black and hydrophobic residues colored in red. Alignment was performed using the Smith-Waterman algorithm.

2.2.3 Substrate recognition by the C-JID

The mode of recognition utilized by the C-JID to detect the foreign protein is reminiscent of the way immunoglobulins bind to their antigen (Fig. 2.4). Loops emerging from the β -sandwich structure target sites in XopQ to form substrate-specific contacts with the pathogen protein in a manner that resembles the complementarity-determining regions found in antibodies. The loop between β -strands 7 and 8 of the ROQ1 C-JID simultaneously recognizes a hydrophobic pocket via the insertion of an isoleucine (I1277^{ROQ1}), and an area of negative potential targeted by R1280^{ROQ1} (Fig. 2.3A). Disrupting these interactions with a ROQ1 double mutant (R1280D and I1277A) prevented HR in tobacco leaves, suggesting that these interactions are essential for XopQ detection by ROQ1 (Supplemental Fig. 1.1A).

The greatest number of contacts between the C-JID and XopQ are made by a 33 residue loop (aa 1163-1196) that dives into the active site cleft of the effector and positions side chains in close contact with conserved sites required for ADPR-binding (Fig. 2.3B) (36). We refer to this loop as the NR loop for its ability to bind residues in XopQ responsible for nucleoside recognition (NR). Two α -helical segments of the loop bring together large hydrophobic side chains that interface with the interior lid region of XopQ (Fig. 2.3B). The conserved XopQ residues targeted in this region (W361^{XopQ}, F366^{XopQ}, L345^{XopQ}) serve to recognize the base moiety of ADPR (36). Active site residues that would otherwise stabilize the α -phosphate of the ligand (Y311^{XopQ} and Y398^{XopQ}) are recognized by ROQ1 V1171^{ROQ1}, H1178^{ROQ1} and H1179^{ROQ1(36)}. Additionally, H1179^{ROQ1} interacts with D120^{XopQ} which is involved in the recognition of one of the sugar moieties in ADPR (36). In summary, the conserved residues in XopQ involved in recognizing the base, α -phosphate and ribose moieties in ADPR are targeted by the ROQ1's NR loop. Mutating the NR loop to a short flexible linker (-SGGGSGGS-) resulted in loss of HR, suggesting the ROQ1 mutant could no longer recognize XopQ (Supplemental Fig. 1.1A). Comparison of our structure of XopQ, which is in an open state, with the closed, ADPR-bound state (PDB: 4P5F), shows that the NR loop overlaps with ADPR and thus would prevent the ligand from entering the active site cleft or interacting with XopQ (Fig. 2.3C). The presence of the NR loop may also block XopQ from transitioning to the closed state, as the NR loop would clash with the lid region capping the active site. These observations lead us to hypothesize that ROQ1 not only recognizes the pathogen effector but may also inhibit its mechanism of ligand binding (52).

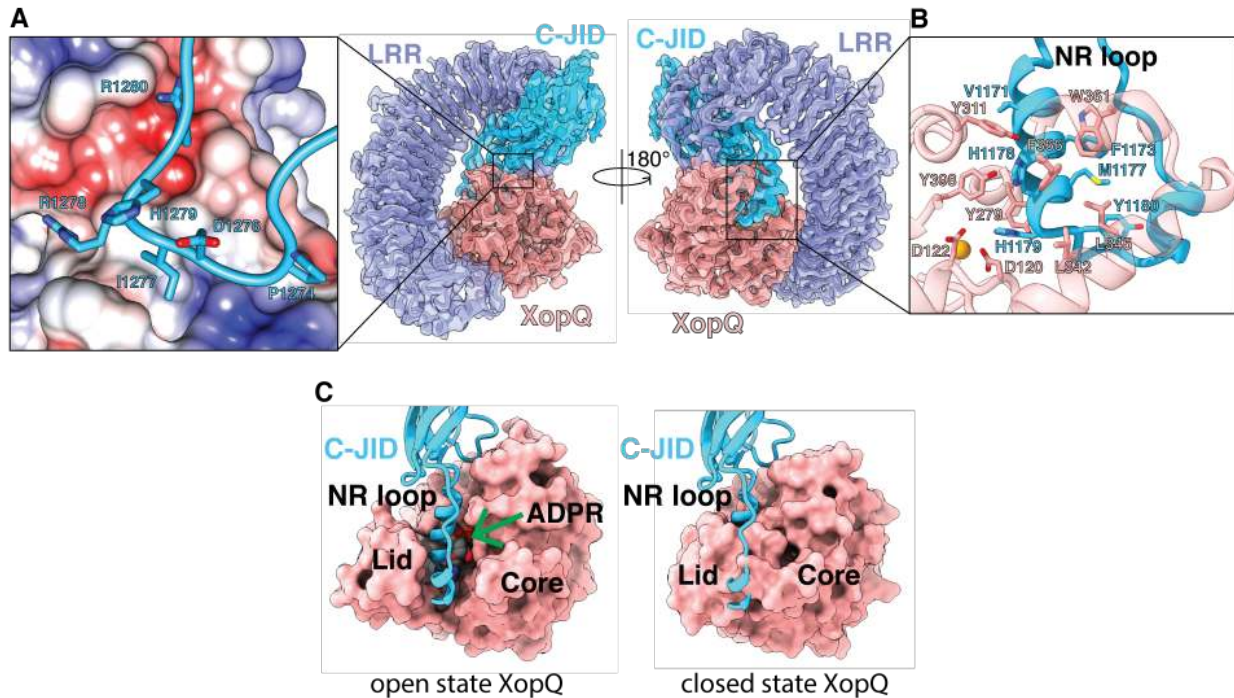


Figure 2.3 Structure of the ROQ1 C-JID (PL domain) binding to XopQ. (A) Surface contacts made by the loop between β -strands 7 and 8 of the C-JID domain (light blue) and XopQ represented by its Coulombic surface potential. (B) Interactions between the NR loop (light blue) and active site residues of XopQ required for ADPR- binding. Catalytic Ca^{2+} shown in gold. (C) Left: Structure of XopQ in the open conformation built from our cryo-EM density, with the NR loop inserted into the active site cleft. The position of ADPR (green arrow) from the close state of XopQ (PDB: 4P5F) is modeled to show its overlapping position with the NR loop. Right: The ADPR-bound, closed state of XopQ. The NR loop is modeled to demonstrate the clashes that would occur upon XopQ closure.

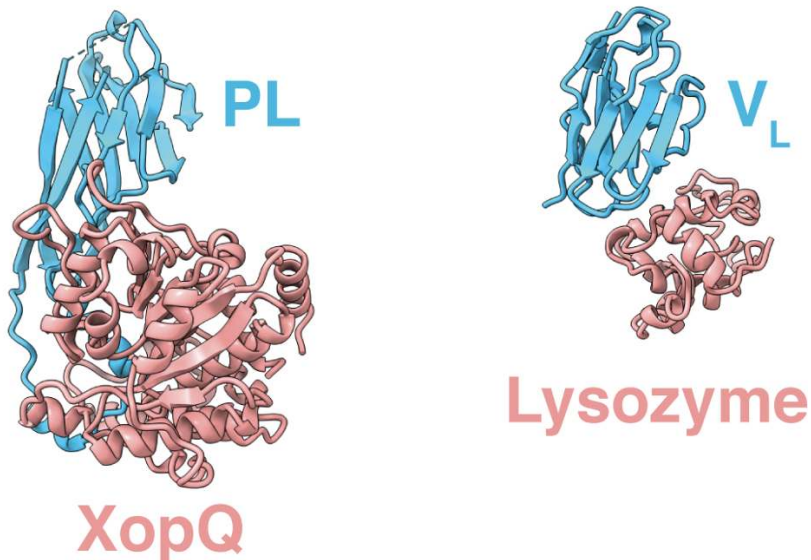


Figure 2.4 Similar mode of recognition utilized by the C-JID and immunoglobulins. Comparison between the C-JID domain of ROQ1 recognizing XopQ (left) and the light-chain variable fragment (V_L) of an antibody recognizing lysozyme (PDB: 3HFM) (right). Loops emerging from the β -sandwich of either the C-JID or V_L (light blue) interact with the substrate (salmon).

2.2.3 Conservation of the ROQ1 C-JID

The C-JID of ROQ1 has a conserved β -sandwich core that may be found in the NLRs of other members of the nightshade family (Figure 2.5). We ran a BLAST search using the sequence of the C-JID (aa 1129-1306) and found multiple hits corresponding to resistance genes in other species of tobacco, as well as in various species of potatoes, peppers and morning-glories. The more conserved residues are within the strands of the β -sandwich, whereas the loop residues pointing towards XopQ are more variable (Fig. 2.5). The NR loop is only found in three other tobacco species, with minor sequence differences (V1171→I, Y1195→F). This pattern of conservation suggests that the variable loops emerging from the C-JID core of related NLRs could serve in recognizing different pathogen effectors via a similar mechanism to that used by ROQ1. Such a strategy would be akin to that of sequence variations in the complementarity-determining regions of antibodies that enable them to recognize a diversity of epitopes.

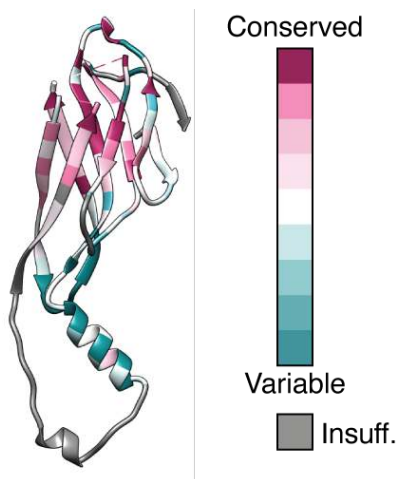


Figure 2.5 Residue conservation of the ROQ1 C-JID. Regions where too few sequences aligned to calculate a reliable conservation score were colored in gray (labeled “Insuff.”).

2.3 Conclusions

Previous studies suggest that it was difficult to identify mutations in XopQ that could evade ROQ1 recognition (53). This is consistent with our results that demonstrate that the LRR and C-JID of ROQ1 make multiple contacts with XopQ, suggesting that this gene may be durable in the field and difficult for the pathogen to evade. In the future, these contacts could be modified to build synthetic receptors targeting various pathogen effectors resulting in novel recognitional specificities.

2.4 Materials and Methods

2.4.1 Cryo-EM data processing

To resolve the interaction between ROQ1 and XopQ, we applied symmetry expansion to our particles and performed a focused refinement using a mask around one LRR-PL-XopQ module. The angular search space was restricted to preserve the particle orientations after symmetry expansion. The resulting reconstruction converged to 3.8 Å resolution, displaying clear separation between β -strand of the LRR and PL, as well as densities for the sidechains that interact with XopQ.

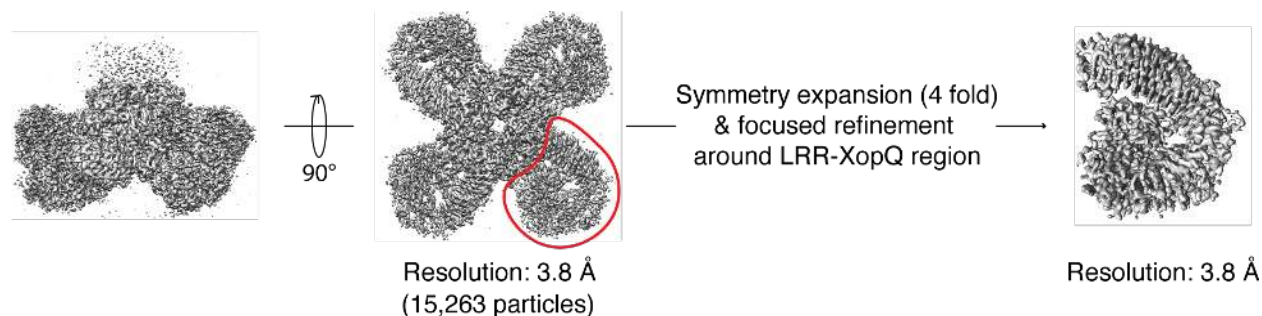


Figure 2.6 Focused refinement of the ROQ1-XopQ interaction region. The masked region for focused refinement is circled in red.

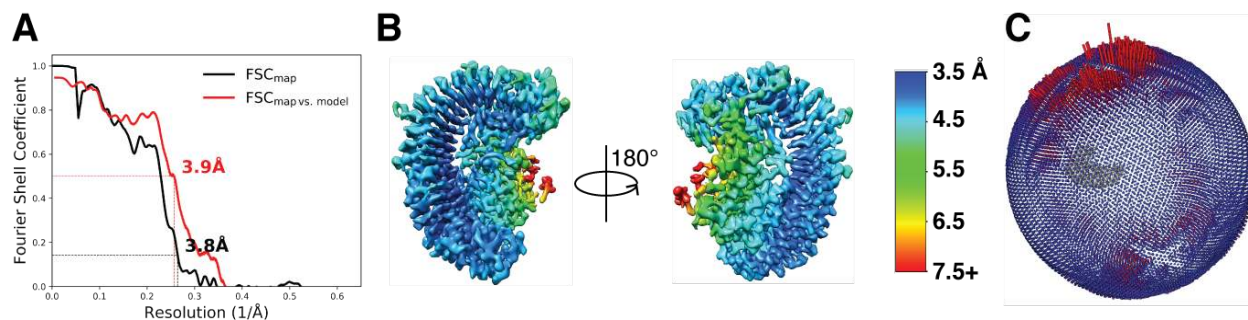


Figure 2.7 Resolution estimation. (A) map FSC and map vs model FSC. **(B)** Cryo-EM density color-coded according to local resolution. **(C)** Angular distribution plots of particles included in the 3D reconstruction.

2.4.2 Model building and refinement

The overlap between our model of ROQ1 (res. 189-625) complex and the map resulting from the focused classification around the LRR-PL-XopQ region was used to build the following C-terminal residues of ROQ1. We used the secondary-structure prediction algorithm in Phyre2 (54) to guide us in building our model, specifically matching densities of β -strands and α -helices to sequences of residues with a corresponding predicted secondary structure. In a few cases, poorly resolved linker regions between β -strands were left unmodeled. We used the densities of large side chains and nearby secondary structure elements to ensure correct register assignment of the residues that followed. The structure of the open conformation of XopQ from *Xanthomonas oryzae pv. oryzae* (PDB: 4KL0) was used to fit XopQ into our density. The minor sequence differences with

XopQ from *Xanthomonas euvesicatoria* were fixed in COOT (43). Models were refined in phenix as described previously in Chapter 1.

2.4.3 Residue conservation in the ROQ1 C-JID

The conservation scores for each residue in the C-JID of Roq1 (1129-1306) were calculated in Consurf (52). Unique homologous sequences with a sequence identity between 20% and 95% were collected from UNIREF90 using 3 iterations of the PSI-BLAST search algorithm (E-value: 0.0001). The 38 unique sequences found were aligned using MAFFT (55). In some regions, too few sequences aligned to calculate a reliable conservation score (positions occupied by fewer than 6 amino acids in the multiple sequence alignment are deemed to have unreliable scores) and were colored in gray. This occurred in our alignment at positions 1179-1200 (corresponding to a part of the NR loop of Roq1 that recognizes XopQ's active site) for which only 2 homologues found were aligned with.

Chapter Three

Oligomerization of ROQ1

Note: These results have been published and are discussed in more detail in our recent paper Martin et al. 2020 (1).

3.1 Introduction

NLRs are generally thought to exist in an inhibited state mediated by either intra- or intermolecular contacts that prevent oligomerization between protomers and activation of the immune response (9, 56). Structural studies of inactive NLRs suggest that these inhibitory contacts hold the nucleotide-binding region (NBD, HD1, WHD) in a closed state (10, 57, 58). Upon activation, these interactions must be disrupted in order to transition to the oligomerization-prone state, where the WHD is moved away from the nucleotide-binding site, thereby displacing the ADP-specific MHD motif on the WHD and allowing ATP binding (11, 32, 59–61).

3.2 Results and Discussion

3.2.1 Auto-inhibition and activation of ROQ1

We expect ROQ1 to be regulated by autoinhibitory contacts with the LRR, based on evidence demonstrating that a truncated version of ROQ1 missing the LRR and C-JID regions spontaneously triggers an immune response in the absence of effectors (20). We sought to determine if the C-JID could play a role in auto-inhibition. Removing the C-JID of ROQ1 (Δ PL) resulted in loss of HR *in planta*, suggesting the LRR, not the C-JID, is involved in making the intramolecular contacts that obstruct a conformational switch to the active state (Supplementary Fig. 1.1A).

Four ROQ1 protomers oligomerize via the NB-ARC domains upon substrate recognition(20). Our density map reveals the molecular contacts between the three subdomains of the NB-ARC (NBD, HD1 and WHD) in the context of the resistosome, as well as the presence of ATP at the nucleotide binding pocket, consistent with an activated state of ROQ1 (Fig. 3.1, 3.2).

3.2.2 ATP-binding

The ATP molecule is stabilized at the interface between the NBD and HD1, with the NBD recognizing the β -phosphate via the canonical P-loop (K224 and T225), with two aspartates (D300 and D301) of the Walker B motif in close proximity to a Mg^{2+} ion that is further coordinated by the β - and γ -phosphate of ATP as well as T225 of the P-loop (Fig. 3.1) (62). Further recognition of the ligand is provided by R329 of TTR motif (aa 327–329) that interacts with the ATP γ -phosphate, and by residues forming a pocket around base moiety (L190, I193, L356). The role of R329 in sensing the ATP molecule is highlighted by a loss of HR phenotype when it is mutated to an alanine (Supplementary Fig. 1.1D).

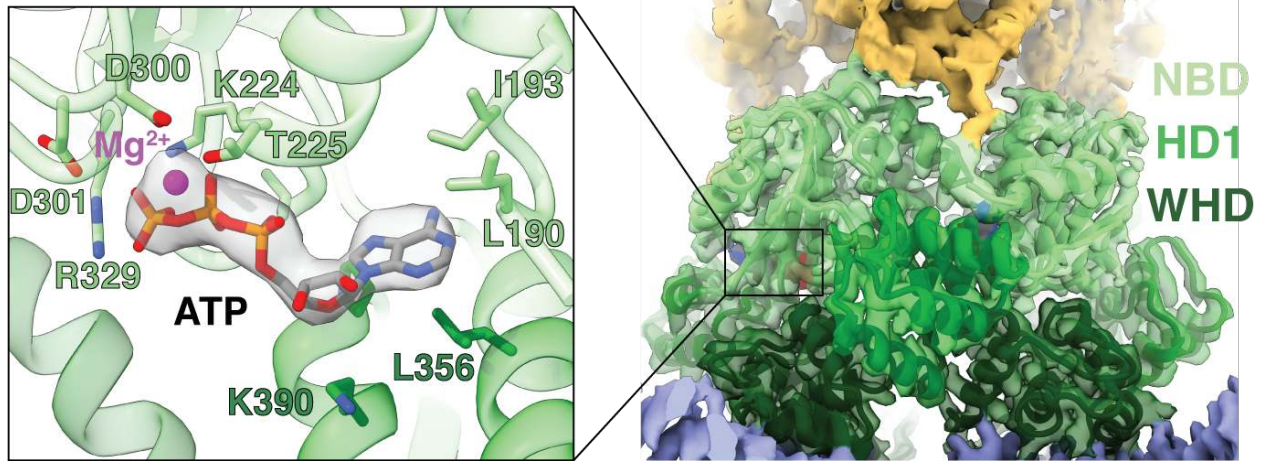


Figure 3.1 The ATP-binding site of the ROQ1 NB-ARC domain. ATP modeled in the cryo-EM density (4.8 σ) at the oligomerization interface, showing the sidechains of residues involved in ATP and Mg²⁺ (magenta) binding.

3.2.3 Oligomerization interface

In agreement with published NLR structures in the active state (11, 32, 59–61), the WHD of activated ROQ1 is rotated away from the nucleotide-binding site, thereby displacing the MHD motif and exposing the oligomerization interface (Fig. 3.2A). This arrangement allows the NBD-HD1 surface of a protomer to intercalate with the NBD-WHD surface of its neighbor. The major interactions involve an HD1-WHD interface and an NBD-NBD interface (Fig. 3.2A). HD1 binds to the neighboring WHD using a mixture of polar and hydrophobic contacts. Residues surrounding the fourth α -helix of HD1 (aa 401–413) play an important role in forming the ROQ1 tetramer (Fig. 3.2A). Single point mutations changing the character of these residues (E399R, V403D and R410A) resulted in loss of HR, suggesting ROQ1 oligomerization was disrupted (Supplementary Fig. 1.1B). Similar results were observed when mutating the charged residues that bring together NBD domains (R229D) (Supplementary Fig. 1.1B). In other structures of multimeric NLRs (11, 32, 59–61), the contacts between the NBDs also involve their N-terminal linker. The equivalent linker in ROQ1 is poorly resolved in our cryo-EM map compared with the surrounding NBD, for which we observe well-defined sidechain densities, indicating that the linker region in ROQ1 is flexible in the tetrameric state. Furthermore, the same linker in other NLRs provides contacts that are in part responsible for properly positioning the NBDs relative to each other. In fact, in NLRs that form larger order oligomers, the linker forms an α -helix, whereas in smaller complexes, such as the pentameric ZAR1, the N-terminal linker forms a slim structured loop without any secondary structure, allowing for the NBD to pack more tightly (Fig. 3.3). Similarly, the poorly defined structure in the ROQ1 linker could explain the tight packing between NBDs that results in tetramerization instead of higher oligomeric states.

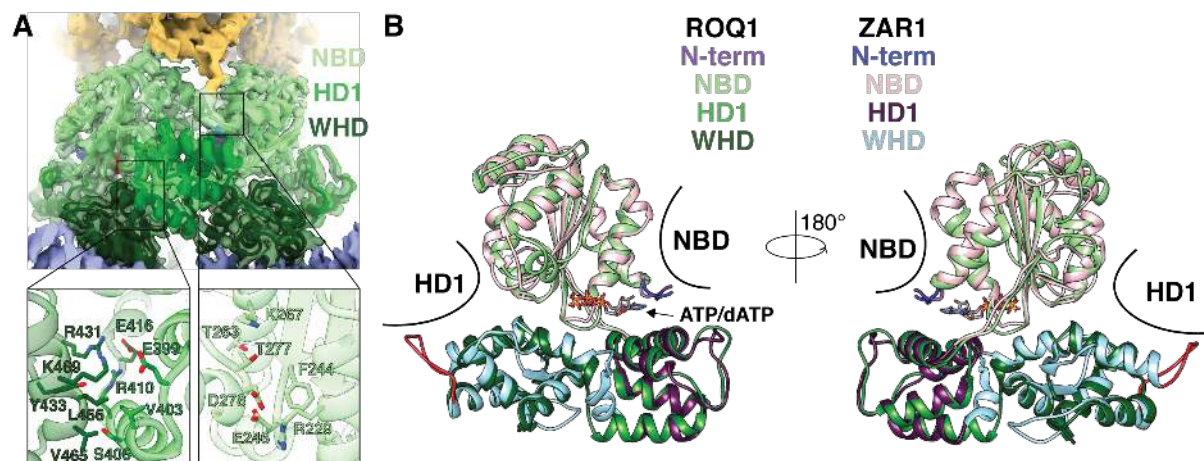


Figure 3.2 Oligomerization interfaces between NB-ARC domains. (A) Interface between two NB-ARC domains of neighboring protomers. Left: Contacts between the WHD and HD. Right: Contacts between neighboring NBDs. **(B)** Structural comparison between the NB-ARC domain of ROQ1 and ZAR1 in the oligomerized state. The NBD and HD1 of neighboring subunits are represented in black. The NBD and HD1 closely align to each other, whereas we find differences in the loops of the WHD, with one of them extending to make contacts with the neighboring HD1 (red). This loop compensates for the increased distance between the WHD and HD1 in the ZAR1 pentamer relative to the ROQ1 tetramer.

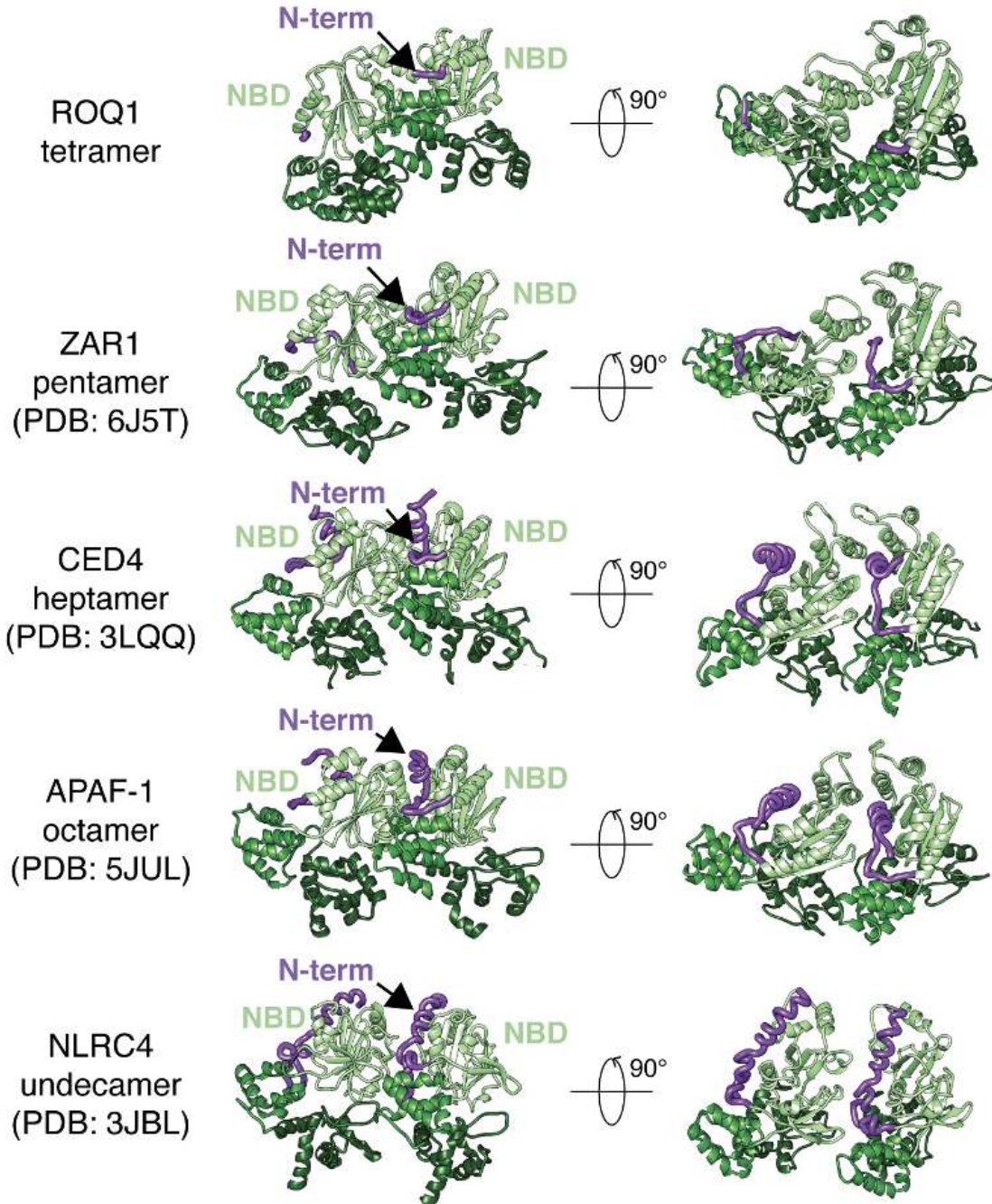


Figure 3.3 Structure of the NBD N-terminal linker in activated NLRs with increasing oligomeric states. The NBD-HD1-WHD of two neighboring protomers is shown (following the color scheme of ROQ1), with the N-terminal linker of the NBD (purple) wedged between them.

3.2.4 Mechanism of oligomerization

Mechanisms have been proposed for the oligomerization of NLRs with differing reliance on nucleotide-binding (56). In the case of ZAR1, indirect substrate recognition mediated

by the guard protein, RKS1, causes a conformational change in the NBD and triggers ADP-release, but the individual ZAR1 protomers are still unable to oligomerize independently of ATP (10, 11). In contrast, the direct recognition of flagellin by the NLR NAIP5 induces a large conformational transition to the active state (32, 63) and has been shown to activate even when the ATP-binding P-loop motif was mutated (64). The structure of the ROQ1 NB-ARC domain closely resembles that of ZAR1 (Fig. 3.2B) and shares a 22.2% sequence similarity. Previous studies have also shown that mutation in the P-loop of ROQ1 prevented oligomerization (20), suggesting ATP-binding is required for assembly. Based on these observations, we expect ROQ1 to follow a similar oligomerization mechanism to ZAR1, in which substrate recognition by the LRR and C-JID of ROQ1 induces a conformational change in the NBD that releases ADP. ATP-binding would then be required to transition to the oligomerization-prone state.

3.3 Conclusions

Our structure of the ROQ1 NB-ARC domain in its oligomerized state is consistent with previously published NLR structures, where contacts between individual protomers are formed between the NBD-HD1 and NBD-WHD interface. Furthermore, the WHD is displaced from the nucleotide binding pocket, allowing the active site residues to bind ATP. The recent structure of RPP1 bound to ATR13 was found in an ADP-bound state, most likely due to mutations in the active site, in which the arginine of the TTR motif was replaced with a glutamic acid (E400^{RPP1}) (51). NLRs differ significantly in the number of protomers required to form the assembled complex. The oligomerization state may depend on the nature of the N-variable domain. For example, the CC domains of ZAR1 must interface in a specific manner in order to form a pore. Another possibility is that the NLR oligomerization state controls its threshold of activation. Previous studies suggest that NLR activation is sensitive to the amount of substrate (65). By requiring more promoters to assemble, the NLR may prevent unwanted spontaneous signaling of the immune response.

3.4 Materials and Methods

Cryo-EM data processing, model building and refinement are previously described in Chapter 1.

Chapter Four

TIR domain association and activation

Note: These results have been published and are discussed in more detail in our recent paper Martin et al. 2020 (1).

4.1 Introduction

Tetramerization of the NB-ARC domains brings the TIR domains into close proximity (Fig. 4.1). The individual TIR domains interact with each other upon resistosome assembly, allowing them to become active NADases and trigger HR (66). The mechanisms for how this association renders TIRs catalytically active remains poorly understood. Many structural studies on TNL have relied on truncated TIR-containing proteins that are missing the subunits driving oligomerization (12, 67–71). Here, we describe a mechanism for TIR association and activation in context of the fully assembled ROQ1 TNL.

4.2 Results and Discussion

4.2.1 TIR domains assemble in a dimer of dimers conformation

Our initial four-fold symmetric reconstruction of ROQ1-XopQ could not clearly resolve the density corresponding to the TIR domains. Further analysis (see Methods) revealed that the four TIR domains do not assemble in a four-fold symmetric fashion but form a two-fold symmetric dimer of dimers. The change in symmetry at the TIR domains highlights the importance for flexibility in the linker that connects them to the NBDs, as discussed previously. After adjusting the symmetry for this region and carrying out focused refinement, the TIR domains reached an overall resolution of 4.6 Å, allowing us to visualize secondary structure elements and trace the polypeptide backbone (Fig. 4.1). The TIR domains are arranged forming two types of interfaces. First, TIR domains engage in a head-to-head, symmetric interaction involving alpha helices the αA and αE_2 of each protomer (nomenclature of TIR structural motifs as in (72)) (Fig. 4.4A,B, shown as interaction between same color protomers). This interface, previously termed AE-interface, is also found in many crystal structures of isolated plant TIR domains, including RPP1, RUN1 and SNC1 (Fig. 4.1D) (12, 67). Consistent with published studies on these plant TNLs, mutating residues in the αA helix of ROQ1 (H30A) disrupts HR and highlights the functional importance of these contacts (Supplementary Fig. 1.1C).

In our structure of ROQ1-XopQ, TIR domains engaged in an AE-AE interaction then further dimerize head-to-tail forming what is described as the BE interface (73) (Figure 4A,C shown as interactions between different color protomers). In the BE interaction the so-called BB-loop (residues between βB and αB) of one TIR domain plugs beneath the loop between αD_3 and αE_1 of the adjacent one (Fig. 4.1C). Previous mutational analyses already demonstrated a functionally important role for the BB-loop in TIR domains (12, 74). We further mutated residues in the αD_3 - αE_1 loop (I151A and G153A) that are in close

contact with the BB-loop and found that they independently resulted in loss of the HR phenotype (Supplementary Fig. 1.1C).

Association between plant TIR domains at the DE surface (formed in part by the αD_3 - αE_1 loop) has previously been observed in crystallographic studies, but their conformations are different from the ones defined by our cryo-EM analysis. For example, the TIR domains of RPP1, SNC1 and L6 face each other head-to-head at their DE surfaces, with different rotational angles relative to each other, instead of interacting in a head-to-tail fashion (67), perhaps because the TIR domains were visualized in isolation and the NB-ARC domain responsible for driving oligomerization was truncated. These studies highlighted the importance of the DE surface in plant TIR domain oligomerization, but the proper interactions remained unclear due to the variability in conformation between structures. The BE-interaction is found in more distant phyla. The crystal structures of TIR domains from the human SARM1 (12) and MAL(75) proteins, as well as TRR-2 (unpublished, PDB: 4W8G and 4W8H) from *Hydra magnipapillata* share a similar BB-loop conformation to that found in the activated ROQ1 tetramer, in which it fits under the αD_3 - αE_1 loop (Fig. 4.1E). This structural relationship suggests shared mechanistic features for TIR domain assembly and activation between animals and plants. In fact, the human SARM1 TIR domains simultaneously form AE and BE interfaces in the crystal lattice (Fig. 4.1D,E) (12).

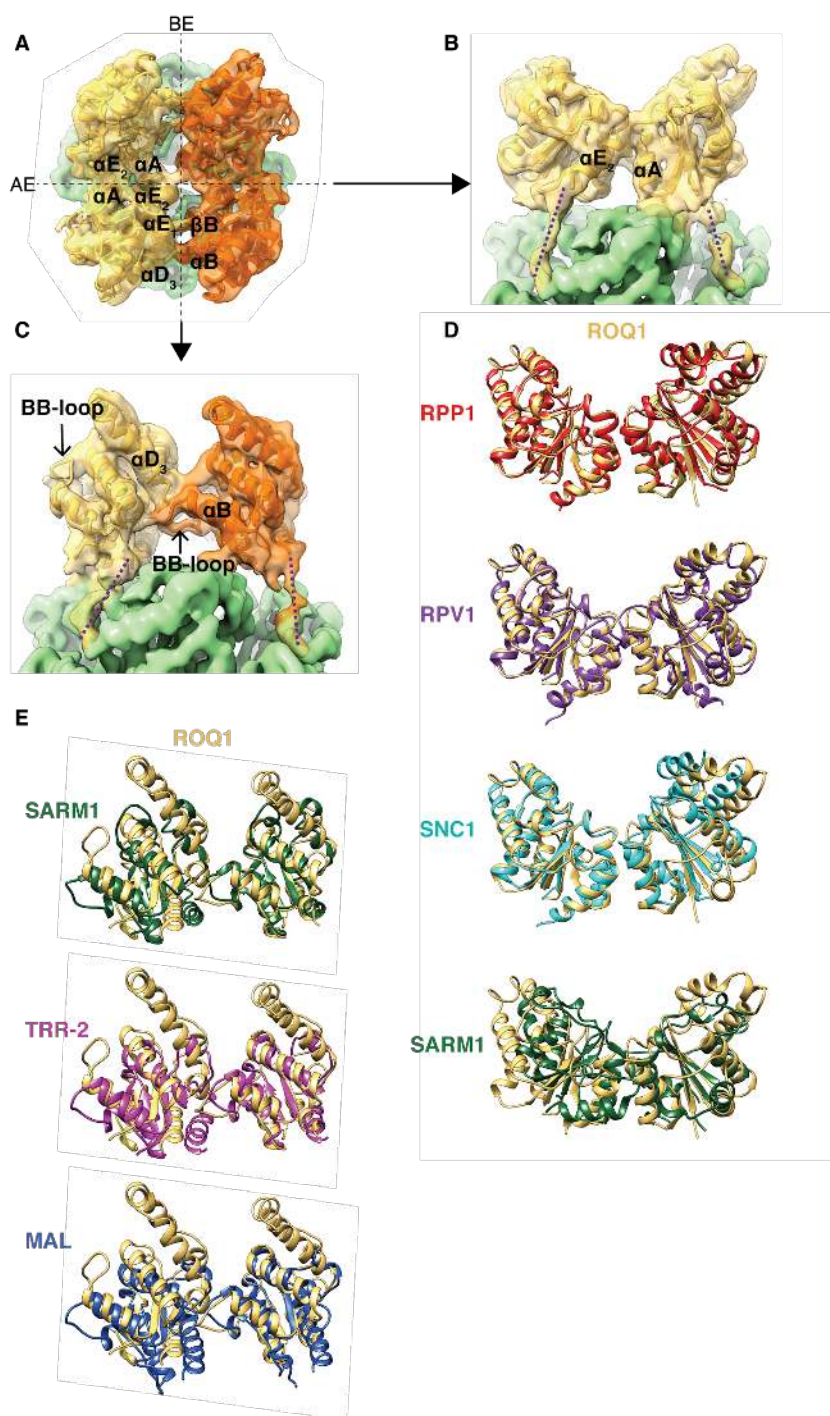


Figure 4.1 TIR domain interfaces. (A) Top view of ROQ1 displaying the four TIR domains organized as a dimer of dimer (each symmetric dimer shown in distinct yellow and orange). The two interfaces are marked with black dotted lines: the AE interface is formed between TIR domains shown in the same color. (B) Orthogonal view from panel A of the AE interface. (C) Orthogonal view from panel A of the BE interface marking the BB-loop positioned under the αD_3 to αE_1 helices. The proposed paths of the protein chain linking the TIR domain to the NBD are drawn with purple dotted lines in panel B and C. (D) Structural comparison between the ROQ1 TIR AE interface and the AE interface found in the crystal lattice of other TIR domains. (E) Structural comparison between the ROQ1 TIR BE interface and the BE interface found in the crystal lattice of metazoan TIR domains. A gaussian filter was applied to the map in (A-C) (width 1.5 Å) in order to reduce noise.

4.2.2 BB-loop conformational rearrangement

Our structure now demonstrates that the BB-loop takes on two different conformations within the activated ROQ1 tetramer and undergoes a conformational switch as TIR domains interact at a BE interface. In the protomer in which the BB-loop is unbound (the one that is contributing to the BE contacts through its DE surface), it is seen in an upward position along the rim of the NADase active site (Fig. 4.2A,B). This conformation is the same as found in the TIR crystal structures lacking BE contacts (67). In the other protomer, the BB-loop interfacing with the adjacent DE surface has been repositioned via a downward motion of about 12 Å (Fig. 4.2B, bottom). A highly conserved glycine residue (G52^{ROQ1}) in the BB-loop likely provides the flexibility required to undergo this conformational switch. Mutating this glycine to a proline resulted in loss of HR (Supplementary Fig. 1.1D). Similarly, mutating the equivalent glycine in SARM1 (G601P) was shown to hinder flexibility and prevent a transition to the engaged state, resulting in a defective BE-interface with the loop stuck in the upward position and a severe decrease in NADase activity (12).

Repositioning of the BB-loop induced by the BE-interface opens the NADase active site (Fig 4D). Large, positively charged side chains (of K50^{ROQ1}, R51^{ROQ1} and K53^{ROQ1}) that would otherwise crowd the entrance of the active site are moved down with the BB-loop. The structure of a SARM1 mutant (G601P), in which the BB-loop is trapped in the unengaged state, reveals a lysine inserted inside the active site cleft; this indicates these sidechains may act to prevent substrate binding (12). Furthermore, NADase activity increased when equivalent BB-loop arginines were mutated to alanines in the plant RUN1 TIR domain (12). Together, these studies suggest that these large positively charged side chains serve to inhibit the NADase function and must be displaced for TIR activation.

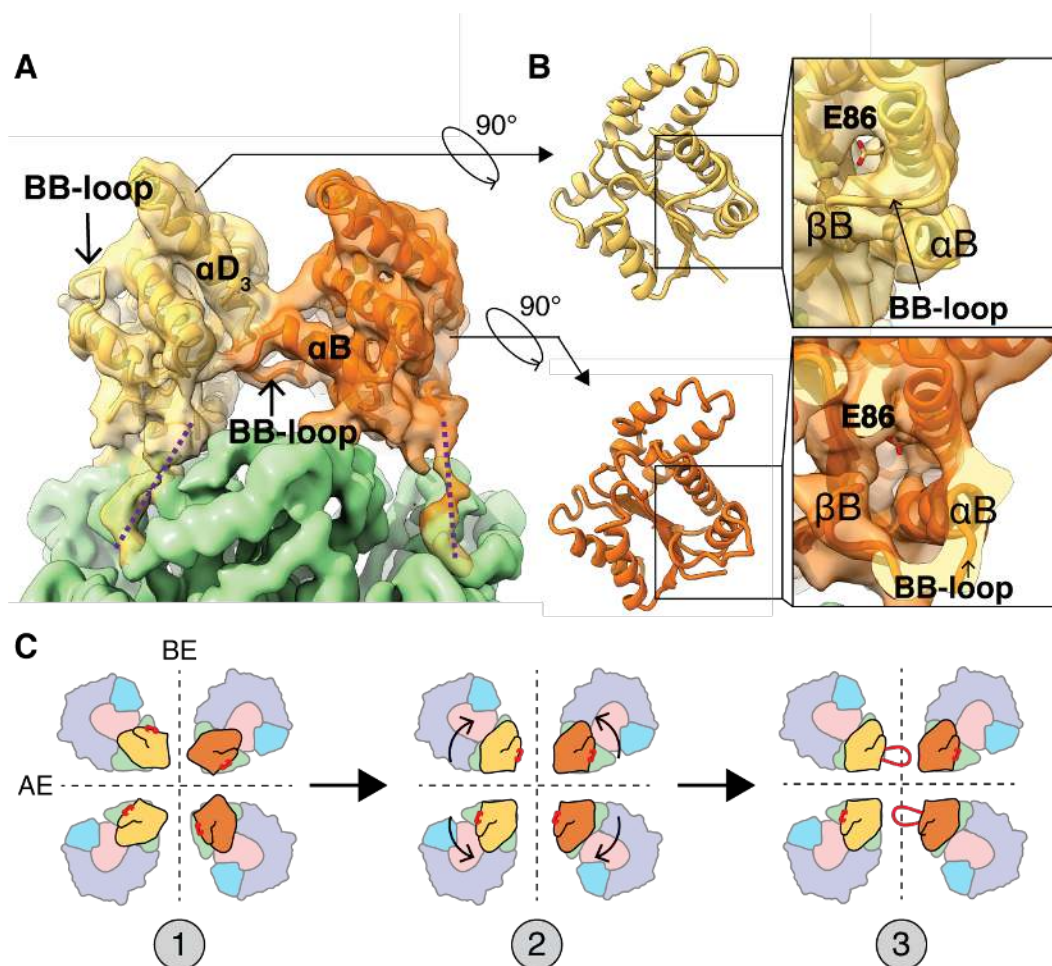


Figure 4.2 TIR domain conformational rearrangement of the BB-loop. (A) The BE interface marking the BB-loop positioned under the αD_3 to αE_1 helices. The proposed paths of the protein chain linking the TIR domain to the NBD are drawn with purple dotted lines. (B) Top: NADase active site of a TIR domain for which the BB-loop is not interfacing with the DE surface. Bottom: Conformational rearrangement in the BB-loop bound to the DE-surface. The side chain of the putative catalytic glutamate (E86) is shown in stick representation. (C) Hypothetical mechanism of TIR oligomerization with the position of the BB-loop in red. (1) Individual TIR domains are brought in close proximity. (2) TIR domains recognize each other at the AE and BE interface. (3) Assembly causes the conformational rearrangement in the BB-loop that opens the NADase active site. A gaussian filter was applied to the map in (A) (width 1.5 Å) in order to reduce noise.

4.2.2 NADase activity

Freeing the active site exposes conserved residues that have been proposed to recognize NAD^+ based on biochemical and structural studies using chemical analogues (12, 13). The nicotinamide moiety of the substrate is supposed to fit in the active site cleft of the TIR domain, bringing the covalently linked ribose in close proximity to the catalytic glutamate. Mutating the putative catalytic glutamate in ROQ1 (E86^{ROQ1}) to an alanine abrogates HR (Supplementary Fig. 1.1D), suggesting loss of NADase activity. No NAD^+ was observed in our structure, which could have been cleaved by the activated TIR domain, yet we still observe a small density that is positioned above the TIR domain active site at the BE interface (Figure 4.3). An ATP molecule was modeled at this position

in Ma et al. (51). The corresponding density in our map is weak compared to that of neighboring residues (W82), with only part of an ATP molecule fitting in the density even at low contour levels (Fig. 4.3B,C). Consequently, it was left unmodeled. Further investigation will be required to determine the position of NAD⁺ within the ROQ1 TIR domain active site. Mechanistic details of NAD⁺ cleavage and product formation remain unresolved and have been found to vary among TIR domains (66). The steps in this enzymatic reaction involve breaking the glycosidic bond that connects nicotinamide to ADPR and, in some cases, a structural rearrangement in ADPR that leads to the formation of cyclic-ADPR or variant-cyclic-ADPR (13, 14). ADPR and cyclic-ADPR have been shown to modulate Ca²⁺ level in plant cells, which is a widely used chemical signal for responding to various biotic and abiotic stresses (15).

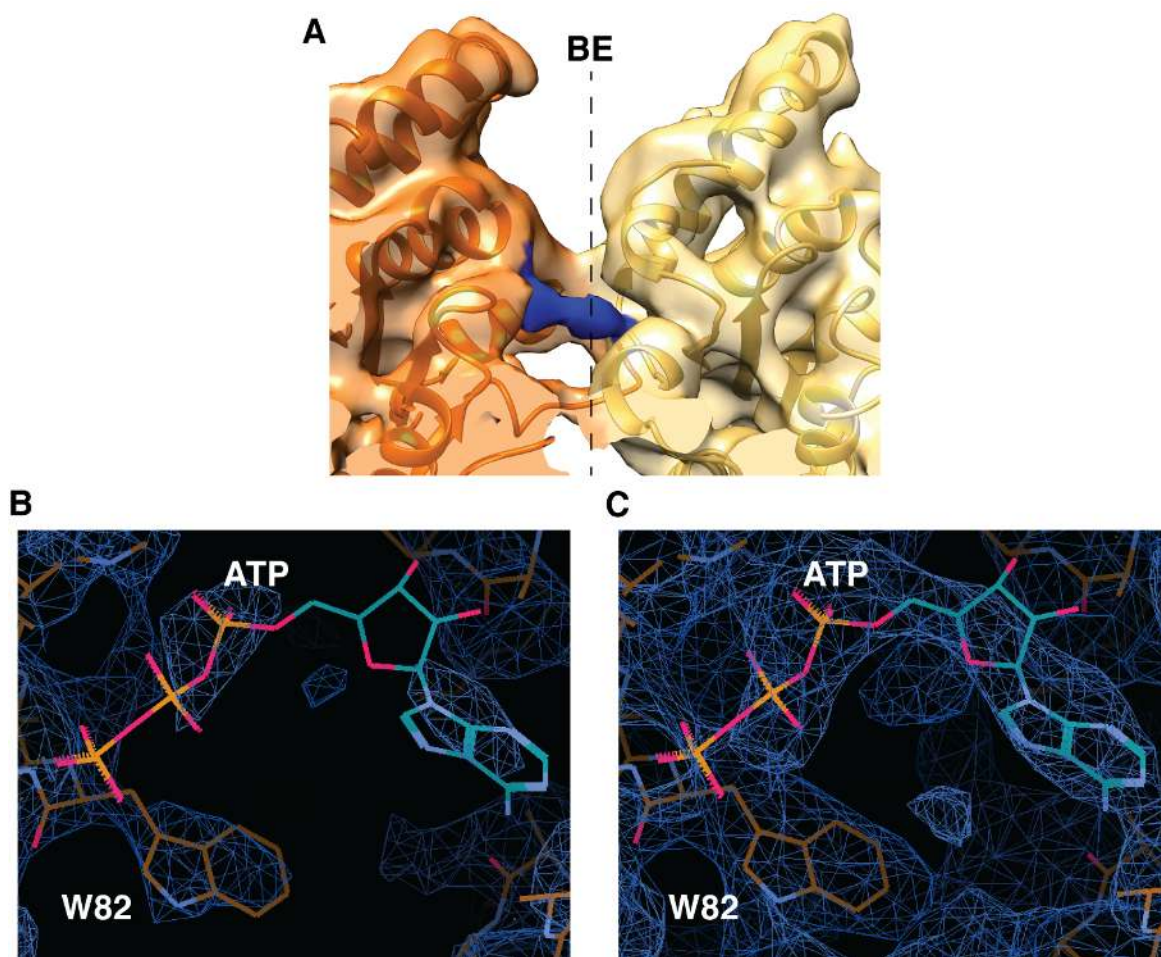


Figure 4.3 A small unidentified density is observed above the TIR domain active site. (A) Two TIR domains at the BE-interface with the unidentified density (blue) in between them. The BB-loop of the TIR domain on the left (orange) is in the engaged state, leaving the NADase active site open. A gaussian filter was applied to the map (width 1.5 Å) to reduce noise. **(B,C)** An ATP molecule was placed within the unidentified density shown at different contour levels. The nearby tryptophan (W82) density can be used to compare signal strength. While density for W82 is clearly visible at low threshold, density for a hypothetical ATP is very weak. At a higher threshold, for which there is density that could account for the base, ribose, α-phosphate and part of the β-phosphate of ATP, the density corresponding to W82 is overblown and noise is visible.

4.3 Conclusions

In the case of the fully assembled ROQ1 TNL, it is clear that the AE and BE interfaces are essential in TIR signaling. Both interfaces align the TIR domains in a conformation conducive to NADase active site opening (Fig. 4.2C). Whether this mechanism of TIR association can be applied to other TNL remains to be determined. Similarly to ROQ1, the TIR domains of the activated RPP1 tetramer form a dimer of dimers via AE and BE-interface contacts causing a rearrangement in the BB-loop (51). Still, there likely exist alternative ways for TIR domains to assemble, based on the number of protomers required to build the active complex, hetero-complex formation with other NLRs, and interface requirements for activation.

4.5 Materials and Methods

4.5.1 Cryo-EM data processing

To improve the TIR domain map, we applied signal subtraction to our particles using a 3D mask around the TIR domains and selected particles exhibiting good density in this region by alignment-free 3D classification. This improved the overall signal for the TIR domain but the features of the density were too poor to confidently fit a model into this four-fold symmetric map. We reasoned that the poor map quality might originate from a symmetry mismatch between the TIR domains and the remainder of the complex, with the TIR domains possibly assuming lower symmetry. Therefore, we applied symmetry expansion to the particles subset and classified the data using alignment-free classification after signal subtraction to remove everything except the TIR domains from the particle images. The particles split equally into two identical classes rotated 90° relative to each other, revealing four TIR domains forming a dimer of dimers with C2 symmetry. Focused refinement of the TIR and NB-ARC regions (the signal from TIR domains alone was too small for proper particle alignment) improved the overall resolution to 4.6 Å, but the NB-ARC region is better resolved than the TIR domains. Based on local resolution estimation, the resolution of the TIR domains is around 7.5 Å, with the highest resolution features observed at the interface between the TIR domains. The onset of phase randomisation leads to an artifact in the corrected half-map FSC curve. For the graphical representation, we have removed three points of the FSC curves near 20 Å resolution to correct for this.

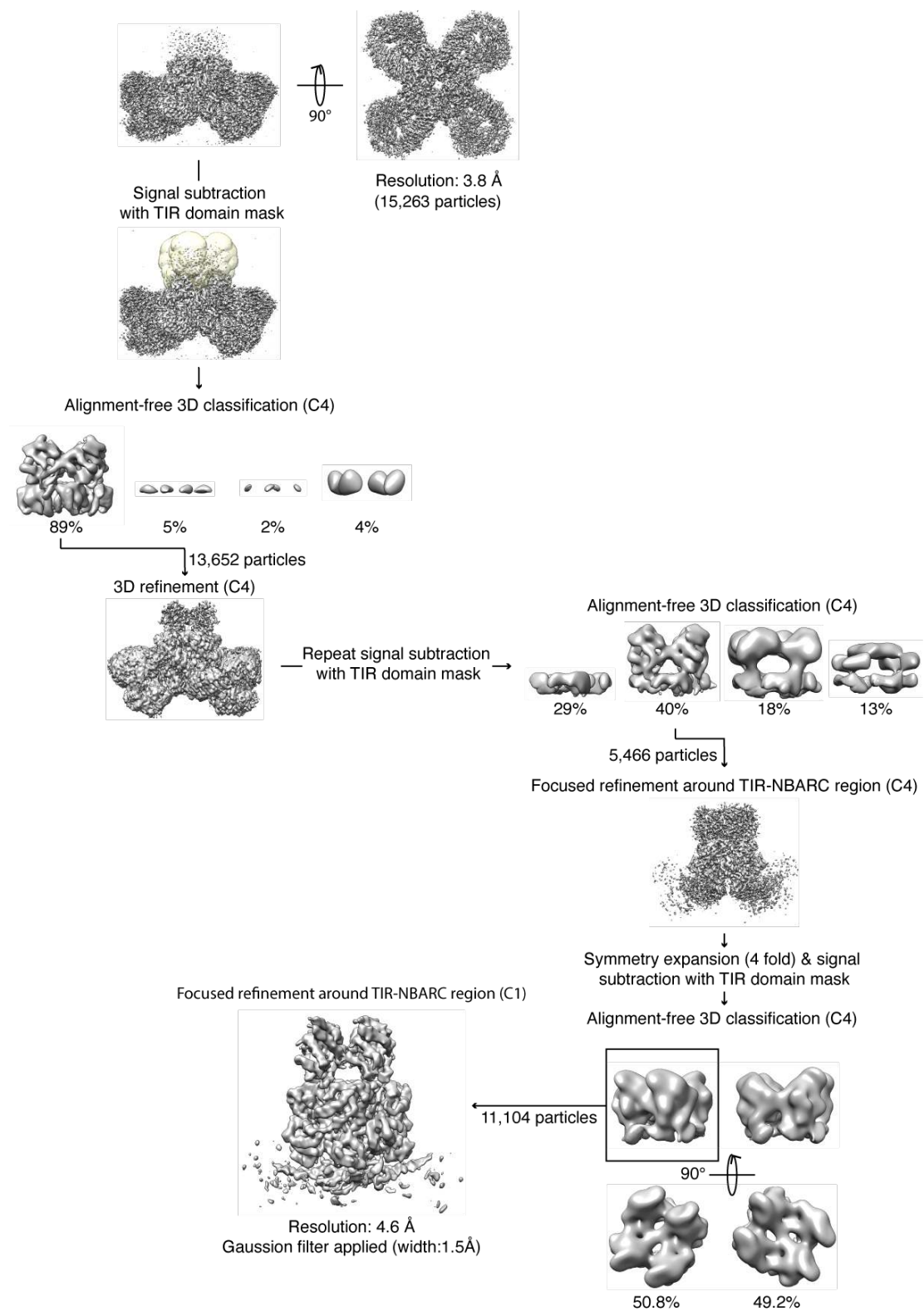


Figure 4.4 Further cryo-EM data processing needed to resolve the TIR domains.

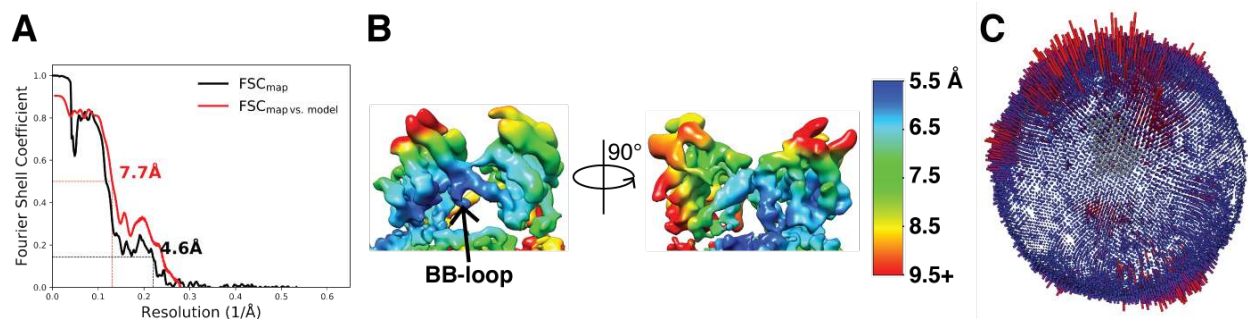


Figure 4.5 Resolution estimation. (A) map FSC and map vs model FSC. (B) Cryo-EM density color-coded according to local resolution. (C) Angular distribution plots of particles included in the 3D reconstruction.

4.5.2 Model building and refinement

A model for the ROQ1 TIR domain was generated in SWISS-MODEL(42) using the structure of the plant RPV1 TIR domain (PDB: 5KU7), as it shares the most sequence similarity among published structures. Four individual TIR domain monomers were docked in the TIR domain map using Chimera(76) and modified in COOT(43) to properly fit the density. Models were refined in phenix as described previously in Chapter 1.

Chapter Five

Final conclusions and outlook

Our structure of the ROQ1-XopQ complex, together with previous biochemical studies, lead us to propose a mechanism for TNL immune signaling: (i) Initially, intramolecular contacts keep the ROQ1 protomer in an auto-inhibited state; (ii) Both the LRR and C-JID recognize the pathogen effector, at which point the NR loop inserts itself into the active site cleft of XopQ and targets conserved residues required for nucleoside-binding; (iii) Recognition of XopQ disrupts the intramolecular contacts in ROQ1 and the NB-ARC domain is released by the LRR; (iv) The NB-ARC domain undergoes a conformational switch to the oligomerization-prone state, in which the WHD is away from the nucleotide-binding pocket, allowing ATP-binding. (v) ROQ1 protomers associate into a four-leaf clover structure and the TIR domains are brought in close contact; (vi) the TIR domains bind to each other forming distinct AE and BE interfaces and causing a conformational rearrangement in the BB-loop of two of the subunits; (vii) the NADase active site is exposed, allowing for the cleavage of NAD⁺.

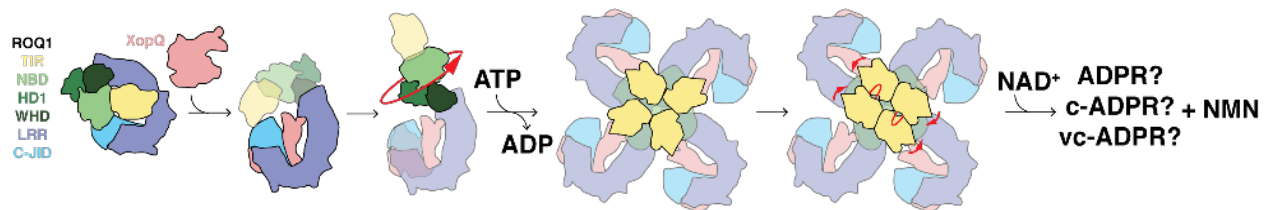


Figure 5 Hypothetical mechanism of ROQ1 activation. From left to right: Auto-inhibited ROQ1 recognizes XopQ; the NB-ARC domain is released and undergoes a conformational switch to the oligomerization-prone state and binds ATP; ROQ1 protomer assemble into a tetramer which brings the TIR domains in close proximity to each other; the TIR domains interfaces via the AE and BE interface causing BB-loop conformational rearrangement and exposure of the NADase active site; cleavage of NAD⁺ results in the production of an ADPR structural isomer and nicotinamide (NMN).

The following steps resulting in the hypersensitive response have yet to be discovered. TIR domains vary in their catalytic activity and products (13). Cleavage of NAD⁺ results in the production of both nicotinamide and an ADPR structural isomer (linear ADPR, cADPR or v-cADPR, which remains uncharacterized). An increase in ADPR levels is correlated with cytosolic calcium influx, which is a widely used response to biotic and abiotic stress in plants, yet, no ADPR-dependent calcium channel has been discovered (77, 78). Some studies suggest that ADPR plays a role in activating downstream regulators of effector-triggered immunity, such as the EDS family proteins (EDS1, SAG101, PAD4) and helper NLRs (NRG1, ADR1). In fact, NRG1 was recently found to localize at the plasma membrane and allow cation influx upon activation (79). Still, no ADPR-binding site has been identified in these downstream regulators. Increasing evidence demonstrates crosstalk between effector- and pattern-triggered immunity in the host in response to pathogen invasion and suggests that these two pathways depend on each other to function effectively (80). Whether ADPR could play a role in this crosstalk remains to be determined.

References

1. R. Martin, T. Qi, H. Zhang, F. Liu, M. King, C. Toth, E. Nogales, B. J. Staskawicz, Structure of the activated ROQ1 resistosome directly recognizing the pathogen effector XopQ. *Science*. **370** (2020), doi:10.1126/science.abd9993.
2. J. Wang, J. Chai, Structural Insights into the Plant Immune Receptors PRRs and NLRs. *Plant Physiol.* **182**, 1566–1581 (2020).
3. J. Tamborski, K. V. Krasileva, Evolution of Plant NLRs: From Natural History to Precise Modifications. *Annu. Rev. Plant Biol.* **71**, 355–378 (2020).
4. Y. Sun, Y.-X. Zhu, P. J. Balint-Kurti, G.-F. Wang, Fine-Tuning Immunity: Players and Regulators for Plant NLRs. *Trends Plant Sci.* **25**, 695–713 (2020).
5. S. Lolle, D. Stevens, G. Coaker, Plant NLR-triggered immunity: from receptor activation to downstream signaling. *Curr. Opin. Immunol.* **62**, 99–105 (2020).
6. J. M. Feehan, B. Castel, A. R. Bentham, J. D. G. Jones, Plant NLRs get by with a little help from their friends. *Curr. Opin. Plant Biol.* **56**, 99–108 (2020).
7. L. M. Jubic, S. Saile, O. J. Furzer, F. El Kasmi, J. L. Dangl, Help wanted: helper NLRs and plant immune responses. *Curr. Opin. Plant Biol.* **50**, 82–94 (2019).
8. S. van Wersch, X. Li, Stronger When Together: Clustering of Plant NLR Disease resistance Genes. *Trends in Plant Science*. **24** (2019), pp. 688–699.
9. J. D. G. Jones, R. E. Vance, J. L. Dangl, Intracellular innate immune surveillance devices in plants and animals. *Science*. **354** (2016), doi:10.1126/science.aaf6395.
10. J. Wang, J. Wang, M. Hu, S. Wu, J. Qi, G. Wang, Z. Han, Y. Qi, N. Gao, H.-W. Wang, J.-M. Zhou, J. Chai, Ligand-triggered allosteric ADP release primes a plant NLR complex. *Science*. **364** (2019), doi:10.1126/science.aav5868.
11. J. Wang, M. Hu, J. Wang, J. Qi, Z. Han, G. Wang, Y. Qi, H. W. Wang, J. M. Zhou, J. Chai, Reconstitution and structure of a plant NLR resistosome conferring immunity. *Science*. **364**, aav5870 (2019).
12. S. Horsefield, H. Burdett, X. Zhang, M. K. Manik, Y. Shi, J. Chen, T. Qi, J. Gilley, J.-S. Lai, M. X. Rank, L. W. Casey, W. Gu, D. J. Ericsson, G. Foley, R. O. Hughes, T. Bosanac, M. von Itzstein, J. P. Rathjen, J. D. Nanson, M. Boden, I. B. Dry, S. J. Williams, B. J. Staskawicz, M. P. Coleman, T. Ve, P. N. Dodds, B. Kobe, NAD cleavage activity by animal and plant TIR domains in cell death pathways. *Science*. **365**, 793–799 (2019).

13. L. Wan, K. Essuman, R. G. Anderson, Y. Sasaki, F. Monteiro, E.-H. Chung, E. Osborne Nishimura, A. DiAntonio, J. Milbrandt, J. L. Dangl, M. T. Nishimura, TIR domains of plant immune receptors are NAD-cleaving enzymes that promote cell death. *Science*. **365**, 799–803 (2019).
14. K. Essuman, D. W. Summers, Y. Sasaki, X. Mao, A. K. Y. Yim, A. DiAntonio, J. Milbrandt, TIR Domain Proteins Are an Ancient Family of NAD -Consuming Enzymes. *Current Biology*. **28** (2018), pp. 421–430.e4.
15. Y. Wu, J. Kuzma, E. Maréchal, R. Graeff, H. C. Lee, R. Foster, N. H. Chua, Absciscic acid signaling through cyclic ADP-ribose in plants. *Science*. **278**, 2126–2130 (1997).
16. Z. Qi, R. Verma, C. Gehring, Y. Yamaguchi, Y. Zhao, C. A. Ryan, G. A. Berkowitz, Ca²⁺ signaling by plant *Arabidopsis thaliana* Pep peptides depends on AtPepR1, a receptor with guanylyl cyclase activity, and cGMP-activated Ca²⁺ channels. *Proc. Natl. Acad. Sci. U. S. A.* **107**, 21193–21198 (2010).
17. W. Tian, C. Hou, Z. Ren, C. Wang, F. Zhao, D. Dahlbeck, S. Hu, L. Zhang, Q. Niu, L. Li, B. J. Staskawicz, S. Luan, A calmodulin-gated calcium channel links pathogen patterns to plant immunity. *Nature*. **572**, 131–135 (2019).
18. X. Yu, G. Xu, B. Li, L. de Souza Vespoli, H. Liu, W. Moeder, S. Chen, M. V. V. de Oliveira, S. Ariádina de Souza, W. Shao, B. Rodrigues, Y. Ma, S. Chhajed, S. Xue, G. A. Berkowitz, K. Yoshioka, P. He, L. Shan, The Receptor Kinases BAK1/SERK4 Regulate Ca²⁺ Channel-Mediated Cellular Homeostasis for Cell Death Containment. *Curr. Biol.* **29**, 3778–3790.e8 (2019).
19. D. Lapin, V. Kovacova, X. Sun, J. A. Dongus, D. Bhandari, P. von Born, J. Bautor, N. Guarneri, J. Rzemieniewski, J. Stuttmann, A. Beyer, J. E. Parker, A Coevolved EDS1-SAG101-NRG1 Module Mediates Cell Death Signaling by TIR-Domain Immune Receptors. *Plant Cell*. **31**, 2430–2455 (2019).
20. T. Qi, K. Seong, D. P. T. Thomazella, J. R. Kim, J. Pham, E. Seo, M.-J. Cho, A. Schultink, B. J. Staskawicz, NRG1 functions downstream of EDS1 to regulate TIR-NLR-mediated plant immunity in. *Proc. Natl. Acad. Sci. U. S. A.* **115**, E10979–E10987 (2018).
21. N. Adlung, H. Prochaska, S. Thieme, A. Banik, D. Blüher, P. John, O. Nagel, S. Schulze, J. Gantner, C. Delker, J. Stuttmann, U. Bonas, Non-host Resistance Induced by the *Xanthomonas* Effector XopQ Is Widespread within the Genus *Nicotiana* and Functionally Depends on EDS1. *Front. Plant Sci.* **7**, 1796 (2016).
22. G. Hu, A. K. A. deHart, Y. Li, C. Ustach, V. Handley, R. Navarre, C.-F. Hwang, B. J. Aegerter, V. M. Williamson, B. Baker, EDS1 in tomato is required for resistance mediated by TIR-class R genes and the receptor-like R gene Ve. *Plant J.* **42**, 376–

391 (2005).

23. H. Cui, K. Tsuda, J. E. Parker, Effector-triggered immunity: from pathogen perception to robust defense. *Annu. Rev. Plant Biol.* **66**, 487–511 (2015).
24. S. U. Huh, V. Cevik, P. Ding, Z. Duxbury, Y. Ma, L. Tomlinson, P. F. Sarris, J. D. G. Jones, Protein-protein interactions in the RPS4/RRS1 immune receptor complex. *PLoS Pathog.* **13**, e1006376 (2017).
25. D. Lapin, D. D. Bhandari, J. E. Parker, Origins and Immunity Networking Functions of EDS1 Family Proteins. *Annu. Rev. Phytopathol.* (2020), doi:10.1146/annurev-phyto-010820-012840.
26. S. Bhattacharjee, M. K. Halane, S. H. Kim, W. Gassmann, Pathogen Effectors Target Arabidopsis EDS1 and Alter Its Interactions with Immune Regulators. *Science*. **334** (2011), pp. 1405–1408.
27. K. Heidrich, L. Wirthmueller, C. Tasset, C. Pouzet, L. Deslandes, J. E. Parker, Arabidopsis EDS1 Connects Pathogen Effector Recognition to Cell Compartment-Specific Immune Responses. *Science*. **334**, 1401–1404 (2011).
28. Y. Zhang, G. Song, N. K. Lal, U. Nagalakshmi, Y. Li, W. Zheng, P.-J. Huang, T. C. Branon, A. Y. Ting, J. W. Walley, S. P. Dinesh-Kumar, TurboID-based proximity labeling reveals that UBR7 is a regulator of N NLR immune receptor-mediated immunity. *Nat. Commun.* **10**, 3252 (2019).
29. A. Schultink, T. Qi, A. Lee, A. D. Steinbrenner, B. Staskawicz, Roq1 mediates recognition of the *Xanthomonas* and *Pseudomonas* effector proteins XopQ and HopQ1. *Plant J.* **92**, 787–795 (2017).
30. N. C. Thomas, C. G. Hendrich, U. S. Gill, C. Allen, S. F. Hutton, A. Schultink, The Immune Receptor Roq1 Confers Resistance to the Bacterial Pathogens , , and in Tomato. *Front. Plant Sci.* **11**, 463 (2020).
31. J. Gantner, J. Ordon, C. Kretschmer, R. Guerois, J. Stuttmann, An EDS1-SAG101 complex functions in TNL-mediated immunity in Solanaceae, , doi:10.1101/511956.
32. J. L. Tenthorey, N. Haloupek, J. R. López-Blanco, P. Grob, E. Adamson, E. Hartenian, N. A. Lind, N. M. Bourgeois, P. Chacón, E. Nogales, R. E. Vance, The structural basis of flagellin detection by NAIP5: A strategy to limit pathogen immune evasion. *Science*. **358**, 888–893 (2017).
33. J. Ryan Feathers, K. A. Spoth, J. Christopher Fromme, Surpassing the physical Nyquist limit to produce super-resolution cryo-EM reconstructions. *Cold Spring Harbor Laboratory* (2019), p. 675397.

34. Y. He, J. Fang, D. J. Taatjes, E. Nogales, Structural visualization of key steps in human transcription initiation. *Nature*. **495**, 481–486 (2013).
35. T. H. D. Nguyen, J. Tam, R. A. Wu, B. J. Greber, D. Toso, E. Nogales, K. Collins, Cryo-EM structure of substrate-bound human telomerase holoenzyme. *Nature*. **557**, 190–195 (2018).
36. S. Yu, I. Hwang, S. Rhee, The crystal structure of type III effector protein XopQ from *Xanthomonas oryzae* complexed with adenosine diphosphate ribose. *Proteins: Struct. Funct. Bioinf.* **82**, 2910–2914 (2014).
37. S. H. W. Scheres, RELION: implementation of a Bayesian approach to cryo-EM structure determination. *J. Struct. Biol.* **180**, 519–530 (2012).
38. S. Q. Zheng, E. Palovcak, J.-P. Armache, K. A. Verba, Y. Cheng, D. A. Agard, MotionCor2: anisotropic correction of beam-induced motion for improved cryo-electron microscopy. *Nat. Methods*. **14**, 331–332 (2017).
39. K. Zhang, Gctf: Real-time CTF determination and correction. *J. Struct. Biol.* **193**, 1–12 (2016).
40. J. Zivanov, T. Nakane, B. O. Forsberg, D. Kimanius, W. J. Hagen, E. Lindahl, S. H. Scheres, New tools for automated high-resolution cryo-EM structure determination in RELION-3. *elife*. **7**, e42166 (2018).
41. A. Punjani, J. L. Rubinstein, D. J. Fleet, M. A. Brubaker, cryoSPARC: algorithms for rapid unsupervised cryo-EM structure determination. *Nat. Methods*. **14**, 290–296 (2017).
42. A. Waterhouse, M. Bertoni, S. Bienert, G. Studer, G. Tauriello, R. Gumienny, F. T. Heer, T. A. P. de Beer, C. Rempfer, L. Bordoli, R. Lepore, T. Schwede, SWISS-MODEL: homology modelling of protein structures and complexes. *Nucleic Acids Res.* **46**, W296–W303 (2018).
43. P. Emsley, K. Cowtan, Coot: model-building tools for molecular graphics. *Acta Crystallogr. D Biol. Crystallogr.* **60**, 2126–2132 (2004).
44. P. D. Adams, R. W. Grosse-Kunstleve, L. W. Hung, T. R. Ioerger, A. J. McCoy, N. W. Moriarty, R. J. Read, J. C. Sacchettini, N. K. Sauter, T. C. Terwilliger, PHENIX: building new software for automated crystallographic structure determination. *Acta Crystallogr. D Biol. Crystallogr.* **58**, 1948–1954 (2002).
45. C. J. Williams, J. J. Headd, N. W. Moriarty, M. G. Prisant, L. L. Videau, L. N. Deis, V. Verma, D. A. Keedy, B. J. Hintze, V. B. Chen, S. Jain, S. M. Lewis, W. B. Arendall 3rd, J. Snoeyink, P. D. Adams, S. C. Lovell, J. S. Richardson, D. C. Richardson, MolProbity: More and better reference data for improved all-atom

- structure validation. *Protein Sci.* **27**, 293–315 (2018).
46. P. V. Afonine, B. P. Klaholz, N. W. Moriarty, B. K. Poon, O. V. Sobolev, T. C. Terwilliger, P. D. Adams, A. Urzhumtsev, New tools for the analysis and validation of cryo-EM maps and atomic models. *Acta Crystallogr D Struct Biol.* **74**, 814–840 (2018).
 47. A. R. Bentham, J. C. De la Concepcion, N. Mukhi, R. Zdrzałek, M. Draeger, D. Gorenkin, R. K. Hughes, M. J. Banfield, A molecular roadmap to the plant immune system. *J. Biol. Chem.* **295**, 14916–14935 (2020).
 48. L. Liu, I. Botos, Y. Wang, J. N. Leonard, J. Shiloach, D. M. Segal, D. R. Davies, Structural basis of toll-like receptor 3 signaling with double-stranded RNA. *Science.* **320**, 379–381 (2008).
 49. C. Van Ghelder, D. Esmenjaud, TNL genes in peach: Insights into the post-LRR domain. *BMC Genomics.* **17**, 1–16 (2016).
 50. I. Sillitoe, N. Dawson, T. E. Lewis, S. Das, J. G. Lees, P. Ashford, A. Tolulope, H. M. Scholes, I. Senatorov, A. Bujan, F. Ceballos Rodriguez-Conde, B. Dowling, J. Thornton, C. A. Orengo, CATH: expanding the horizons of structure-based functional annotations for genome sequences. *Nucleic Acids Res.* **47**, D280–D284 (2019).
 51. S. Ma, D. Lapin, L. Liu, Y. Sun, W. Song, X. Zhang, E. Logemann, D. Yu, J. Wang, J. Jirschitzka, Z. Han, P. Schulze-Lefert, J. E. Parker, J. Chai, Direct pathogen-induced assembly of an NLR immune receptor complex to form a holoenzyme. *Science.* **370** (2020), doi:10.1126/science.abe3069.
 52. W. Li, Y.-H. Chiang, G. Coaker, The HopQ1 Effector’s Nucleoside Hydrolase-Like Domain Is Required for Bacterial Virulence in Arabidopsis and Tomato, but Not Host Recognition in Tobacco. *PLoS ONE.* **8**, e59684 (2013).
 53. N. Adlung, U. Bonas, Dissecting virulence function from recognition: cell death suppression in *Nicotiana benthamiana* by XopQ/HopQ1-family effectors relies on EDS1-dependent immunity. *Plant J.* **91**, 430–442 (2017).
 54. L. A. Kelley, S. Mezulis, C. M. Yates, M. N. Wass, M. J. E. Sternberg, The Phyre2 web portal for protein modeling, prediction and analysis. *Nat. Protoc.* **10**, 845–858 (2015).
 55. K. Katoh, D. M. Standley, MAFFT multiple sequence alignment software version 7: improvements in performance and usability. *Mol. Biol. Evol.* **30**, 772–780 (2013).
 56. Y. Xiong, Z. Han, J. Chai, Resistosome and inflammasome: platforms mediating innate immunity. *Curr. Opin. Plant Biol.* **56**, 47–55 (2020).

57. J. F. C. Steele, R. K. Hughes, M. J. Banfield, Structural and biochemical studies of an NB-ARC domain from a plant NLR immune receptor. *PLoS One*. **14**, 1–20 (2019).
58. Z. Hu, C. Yan, P. Liu, Z. Huang, R. Ma, C. Zhang, R. Wang, Y. Zhang, F. Martinon, D. Miao, H. Deng, J. Wang, J. Chang, J. Chai, Crystal structure of NLRC4 reveals its autoinhibition mechanism. *Science*. **341**, 172–175 (2013).
59. Y. Pang, X. C. Bai, C. Yan, Q. Hao, Z. Chen, J. W. Wang, S. H. W. Scheres, Y. Shi, Structure of the apoptosome: Mechanistic insights into activation of an initiator caspase from *Drosophila*. *Genes and Development*. **29**, 277–287 (2015).
60. S. Qi, Y. Pang, Q. Hu, Q. Liu, H. Li, Y. Zhou, T. He, Q. Liang, Y. Liu, X. Yuan, G. Luo, H. Li, J. Wang, N. Yan, Y. Shi, Crystal structure of the *Caenorhabditis elegans* apoptosome reveals an octameric assembly of CED-4. *Cell*. **141**, 446–457 (2010).
61. L. Zhang, S. Chen, J. Ruan, J. Wu, A. B. Tong, Q. Yin, Y. Li, L. David, A. Lu, W. L. Wang, C. Marks, Q. Ouyang, X. Zhang, Y. Mao, H. Wu, Cryo-EM structure of the activated NAIP2-NLRC4 inflammasome reveals nucleated polymerization. *Science*. **350**, 404–409 (2015).
62. V. Bonardi, K. Cherkis, M. T. Nishimura, J. L. Dargatzidis, A new eye on NLR proteins: focused on clarity or diffused by complexity? *Curr. Opin. Immunol.* **24**, 41–50 (2012).
63. X. Yang, F. Yang, W. Wang, G. Lin, Z. Hu, Z. Han, Y. Qi, L. Zhang, J. Wang, S.-F. Sui, J. Chai, Structural basis for specific flagellin recognition by the NLR protein NAIP5. *Cell Res.* **28**, 35–47 (2018).
64. E. F. Halff, C. A. Diebolder, M. Versteeg, A. Schouten, T. H. C. Brondijk, E. G. Huizinga, Formation and structure of a NAIP5-NLRC4 inflammasome induced by direct interactions with conserved N- and C-terminal regions of flagellin. *J. Biol. Chem.* **287**, 38460–38472 (2012).
65. Z. Duxbury, S. Wang, C. I. MacKenzie, J. L. Tenthorey, X. Zhang, S. U. Huh, L. Hu, L. Hill, P. M. Ngou, P. Ding, J. Chen, Y. Ma, H. Guo, B. Castel, P. N. Moschou, M. Bernoux, P. N. Dodds, R. E. Vance, J. D. G. Jones, Induced proximity of a TIR signaling domain on a plant-mammalian NLR chimera activates defense in plants. *Proc. Natl. Acad. Sci. U. S. A.* **117**, 18832–18839 (2020).
66. A. M. Bayless, M. T. Nishimura, Enzymatic Functions for Toll/Interleukin-1 Receptor Domain Proteins in the Plant Immune System. *Front. Genet.* **11**, 539 (2020).
67. X. Zhang, M. Bernoux, A. R. Bentham, T. E. Newman, T. Ve, L. W. Casey, T. M. Raaymakers, J. Hu, T. I. Croll, K. J. Schreiber, B. J. Staskawicz, P. A. Anderson, K.

- H. Sohn, S. J. Williams, P. N. Dodds, B. Kobe, Multiple functional self-association interfaces in plant TIR domains. *Proc. Natl. Acad. Sci. U. S. A.* **114**, E2046–E2052 (2017).
68. S. J. Williams, K. H. Sohn, L. Wan, M. Bernoux, P. F. Sarris, C. Segonzac, T. Ve, Y. Ma, S. B. Saucet, D. J. Ericsson, L. W. Casey, T. Lonhienne, D. J. Winzor, X. Zhang, A. Coerdet, J. E. Parker, P. N. Dodds, B. Kobe, J. D. G. Jones, Structural basis for assembly and function of a heterodimeric plant immune receptor. *Science*. **344**, 299–303 (2014).
 69. K.-G. Hyun, Y. Lee, J. Yoon, H. Yi, J.-J. Song, Crystal structure of Arabidopsis thaliana SNC1 TIR domain. *Biochem. Biophys. Res. Commun.* **481**, 146–152 (2016).
 70. M. Bernoux, T. Ve, S. Williams, C. Warren, D. Hatters, E. Valkov, X. Zhang, J. G. Ellis, B. Kobe, P. N. Dodds, Structural and Functional Analysis of a Plant Resistance Protein TIR Domain Reveals Interfaces for Self-Association, Signaling, and Autoregulation. *Cell Host Microbe*. **9**, 200–211 (2011).
 71. R. Panstruga, M. J. Banfield, F. L. W. Takken, T. Kroj, S. J. Williams, B. Kobe, L. Yin, G. Foley, L. W. Casey, M. A. Outram, D. J. Ericsson, J. Lu, M. Boden, I. B. Dry, Structure and Function of the TIR Domain from the Grape NLR Protein RPV1. *Front. Plant Sci.* **7**, 1850 (2016).
 72. Y. Xu, X. Tao, B. Shen, T. Horng, R. Medzhitov, J. L. Manley, L. Tong, Structural basis for signal transduction by the Toll/interleukin-1 receptor domains. *Nature*. **408**, 111–115 (2000).
 73. S. Nimma, T. Ve, S. J. Williams, B. Kobe, Towards the structure of the TIR-domain signalosome. *Curr. Opin. Struct. Biol.* **43**, 122–130 (2017).
 74. L. Vyncke, C. Bovijn, E. Pauwels, T. Van Acker, E. Ruysinck, E. Burg, J. Tavernier, F. Peelman, Reconstructing the TIR Side of the Myddosome: A Paradigm for TIR-TIR Interactions. *Structure*. **24**, 437–447 (2016).
 75. T. Ve, P. R. Vajjhala, A. Hedger, T. Croll, F. DiMaio, S. Horsefield, X. Yu, P. Lavrencic, Z. Hassan, G. P. Morgan, A. Mansell, M. Mobli, A. O’Carroll, B. Chauvin, Y. Gambin, E. Sierecki, M. J. Landsberg, K. J. Stacey, E. H. Egelman, B. Kobe, Structural basis of TIR-domain-assembly formation in MAL- and MyD88-dependent TLR4 signaling. *Nat. Struct. Mol. Biol.* **24**, 743–751 (2017).
 76. E. F. Pettersen, T. D. Goddard, C. C. Huang, G.S. Couch, D. M. Greenblatt, E.C. Meng, T. E. Ferrin, UCSF Chimera—a visualization system for exploratory research and analysis. *J Comp Chem*. **25**, 1605–1612 (2004).
 77. R. Fliegert, A. Gasser, A. H. Guse, Regulation of calcium signalling by adenine-

- based second messengers. *Biochem. Soc. Trans.* **35**, 109–114 (2007).
78. Q. Liu, R. Graeff, I. A. Kriksunov, H. Jiang, B. Zhang, N. Oppenheimer, H. Lin, B. V. L. Potter, H. C. Lee, Q. Hao, Structural basis for enzymatic evolution from a dedicated ADP-ribosyl cyclase to a multifunctional NAD hydrolase. *J. Biol. Chem.* **284**, 27637–27645 (2009).
79. P. Jacob, N. H. Kim, F. Wu, F. El-Kasmi, W. G. Walton, O. J. Furzer, A. D. Lietzen, S. Sunil, K. Kempthorn, M. R. Redinbo, Z.-M. Pei, L. Wan, J. L. Dangl, The plant immune receptors NRG1.1 and ADR1 are calcium influx channels. *Cold Spring Harbor Laboratory* (2021), p. 2021.02.25.431980.
80. M. Yuan, B. P. M. Ngou, P. Ding, X.-F. Xin, PTI-ETI crosstalk: an integrative view of plant immunity. *Curr. Opin. Plant Biol.* **62**, 102030 (2021).